

AD-A121 037

ANALYSIS OF SHEAR FROM OCEAN CURRENT METERS(U) SCIENCE
APPLICATIONS INC MCLEAN VA D M RUBENSTEIN ET AL.
MAY 82 SAI-82-687-WA N00014-81-C-0075

1/1

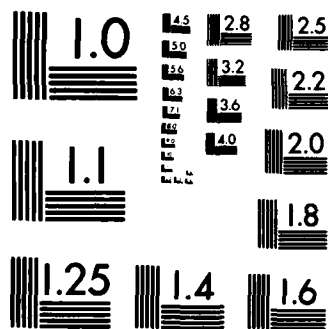
UNCLASSIFIED

F/G 8/3

NL

END

FILMED
FOR
DTIC



MICROCOPY RESOLUTION TEST CHART
NATIONAL BUREAU OF STANDARDS-1963-A

ANALYSIS OF SHEAR
FROM OCEAN CURRENT METERS

SAI-82-687-WA

(12)

AD A 121037

DTIC
ELECTED
NOV 3 1982
H

DTIC FILE COPY

DISTRIBUTION STATEMENT A
Approved for Public Release
Distribution Unlimited

SCIENCE APPLICATIONS, INC.

04 11 08 000

ANALYSIS OF SHEAR
FROM OCEAN CURRENT METERS

SAI-82-687-WA

(12)

DTIC
ELECTE
NOV 3 1982
H



SCIENCE APPLICATIONS, INC.

Post Office Box 1303, 1710 Goodridge Drive, McLean, Virginia 22102, (703) 821-4300

DISTRIBUTION STATEMENT A
Approved for public release:
Distribution Unlimited

UNCLASSIFIED

SECURITY CLASSIFICATION OF THIS PAGE (When Data Entered)

REPORT DOCUMENTATION PAGE		READ INSTRUCTIONS BEFORE COMPLETING FORM
1. REPORT NUMBER SAI-82-687-WA	2. GOVT ACCESSION NO. AD-A121037	3. REPORTING CATALOG NUMBER
4. TITLE (and Subtitle) Analysis of Shear from Ocean Current Meters	5. TYPE OF REPORT & PERIOD COVERED Technical Report 11/80 - 5/82	
7. AUTHOR(s) David M. Rubenstein Fred C. Newman	6. PERFORMING ORG. REPORT NUMBER SAI-82-687-WA	
8. PERFORMING ORGANIZATION NAME AND ADDRESS Science Applications, Inc. 1710 Goodridge Drive, P. O. Box 1303 McLean, VA 22102	9. CONTRACT OR GRANT NUMBER(s) N00014-81-C-0075	
11. CONTROLLING OFFICE NAME AND ADDRESS NORDA Code 540 Ocean Measurements Program NSTL Station, Bay St. Louis, MS 39529	10. PROGRAM ELEMENT, PROJECT, TASK AREA & WORK UNIT NUMBERS	
14. MONITORING AGENCY NAME & ADDRESS (if different from Controlling Office)	12. REPORT DATE May 1982	
	13. NUMBER OF PAGES 92	
	15. SECURITY CLASS. (of this report) UNCLASSIFIED	
	15a. DECLASSIFICATION/DOWNGRADING SCHEDULE	
16. DISTRIBUTION STATEMENT (of this Report) Approved for public release: distribution unlimited.		
17. DISTRIBUTION STATEMENT (of the abstract entered in Block 20, if different from Report) Approved for public release: distribution unlimited.		
18. SUPPLEMENTARY NOTES		
19. KEY WORDS (Continue on reverse side if necessary and identify by block number) Vertical Shear Shear Current Meter Inertial Oscillations Upper Ocean Shear		
20. ABSTRACT (Continue on reverse side if necessary and identify by block number) Current meter records obtained over 48 days from a triangular array of three moorings located near 39°N, 70°W in 1970 are used to investigate the time-variability of vertical shear. Vertical resolution is limited to 20 meters, the separation of the current meters, within the depth interval between 12m and 72m from the surface. Vertical, horizontal, and slant coherences were calculated, as well as frequency spectra. The shear is dominated by the near-inertial frequencies, and the		

DD FORM 1 JAN 73 1473

EDITION OF 1 NOV 65 IS OBSOLETE
5/91 0102-1F-014-4501

UNCLASSIFIED

SECURITY CLASSIFICATION OF THIS PAGE (When Data Entered)

UNCLASSIFIED

SECURITY CLASSIFICATION OF THIS PAGE (When Data Entered)

corresponding amplitudes decay rapidly with depth. Evidence for downward (upward phase) propagation of the inertial shear is presented, and in addition, some evidence for nonlinear interactions between inertial and tidal motions were observed. Significant shear at semidiurnal frequencies was observed at this location due to interaction of the semidiurnal tide with the nearby continental slope.

Accession	
NTIS	
DTIC	
Uncl	
JAN	
By	
Distribution	
Avail Codes	
or	
Dist	
A	

DTIC
COPY
INSPECTED

UNCLASSIFIED

SECURITY CLASSIFICATION OF THIS PAGE (When Data Entered)

ANALYSIS OF SHEAR
FROM OCEAN CURRENT METERS

SAI-82-687-WA

OPD-TR-81-257-03

May 1982

Prepared by:
David M. Rubenstein
Fred C. Newman

Prepared for:
Ocean Measurements Program
Naval Ocean Research and
Development Activity
Code 540
NSTL Station
Bay St. Louis, MS 39529

Contract # N00014-81-C-0075

SCIENCE APPLICATIONS, INC.

1710 Goodridge Drive
P. O. Box 1303
McLean, VA 22102
(703)821-4300



TABLE OF CONTENTS

<u>Section</u>	<u>Page</u>
1 INTRODUCTION AND BACKGROUND	1-1
1.1 Introduction	1-1
1.2 Background	1-7
1.3 The Geodyne 850 Current Meter	1-7
2 STATISTICS PROCEDURES	2-1
2.1 Power Spectral Densities	2-1
2.2 Vector Coherence Spectral Functions	2-3
2.3 Normalized Correlation Functions	2-4
3 POWER SPECTRA	3-1
3.1 Forcing Mechanisms	3-1
3.1.1 Near-Inertial Oscillations	3-1
3.1.2 Semi-Diurnal Oscillations	3-2
3.1.3 Low Frequency Motions	3-4
3.1.4 Internal Wave Band	3-4
3.2 Velocity Spectra	3-5
3.3 Shear Spectra	3-7
3.3.1 Results	3-7
3.3.2 Inertial and Tidal Shear	3-13
3.3.3 Aliasing in the Internal Wave Band	3-14
3.3.4 Dissipation of Inertial Oscillations	3-15
4 COHERENCE SPECTRA	4-1
4.1 Horizontal Coherences	4-1
4.2 Vertical Coherences	4-6
4.3 Wind Stress/Shear Coherences	4-6
4.4 Coherence Analysis	4-8

TABLE OF CONTENTS (Continued)

<u>Section</u>	<u>Page</u>
5 CORRELATION FUNCTIONS	5-1
5.1 Auto-Correlations of Vertical Shear	5-1
5.2 Cross-Correlations of Horizontally, Slant, and Vertically Separated Vertical Shear	5-3
5.3 Cross-Correlation Analysis	5-3
6 SUMMARY AND CONCLUSIONS	6-1
REFERENCES	R-1

LIST OF FIGURES

<u>Figure</u>		<u>Page</u>
1.1	Deployment of moorings in the vicinity of Site D	1-3
1.2	Distribution of data during Summer, 1970	1-4
1.3	Schematic diagram of mooring, from Pollard and Tarbell (1975)	1-5
1.4	Brunt-Vaisala frequency at the three moorings on 9 and 23/24 July and 16/17 August as functions of depth in the top 100 m	1-6
2.1	Frequency response $W(f)$ for a Hanning window function	2-2
3.1	Profile of relief along 70°W (see Figure 1.1 for local isobaths) together with selected semidiurnal characteristics passing near site D (Regal and Wunsch, 1973)	3-3
3.2	Spectra of all records in the top 100 m using 1024 h of data between 28 June and 10 August ...	3-6
3.3	Power spectrum of vertical shear, current meters 3393-3394, at depths 12 and 32 m, respectively	3-9
3.4	As in Figure 3.3, except for meters 3402-3403	3-9
3.5	Power spectrum of vertical shear, current meters 3394-3395, at depths 32 and 52 m, respectively	3-10
3.6	As in Figure 3.5, except for meters 3403-3404	3-10
3.7	Power spectrum of vertical shear, current meters 3385-3386, at depths 52 and 72 m, respectively	3-11
3.8	As in Figure 3.7, except for meters 3395-3396	3-11

LIST OF FIGURES (Continued)

<u>Figure</u>	<u>Page</u>
3.9 Power spectrum of vertical shear, current meters 3404-3406, at depths 52 and 72 m, respectively	3-11
3.10 Garrett and Munk horizontal velocity spectral model (GM79) frequency dependence $f_u(\omega) \propto (\omega^2 + f^2)\omega^{-3}(\omega^2 - f^2)^{-1}$, in variance preserving form	3-16
4.1 Horizontally separated vertical shear coherence amplitudes and phases between 3393-3394 and 3402-3403	4-3
4.2 As in Figure 4.1, except for meters 3394-3395 and 3403-3404	4-3
4.3 As in Figure 4.1, except for meters 3395-3396 and 3404-3406	4-4
4.4 As in Figure 4.1, except for meters 3395-3396 and 3385-3386	4-4
4.5 As in Figure 4.1, except for meters 3404-3406 and 3385-3386	4-5
4.6 Wind stress/vertical shear coherence amplitudes and phases between 3391 and 3393-3394	4-9
4.7 As in Figure 4.19, except for meters between 3401 and 3402-3403	4-9
4.8 As in Figure 4.19, except for meters between 3391 and 3394-3395	4-10
4.9 As in Figure 4.19, except for meters between 3401 and 3403-3404	4-10
4.10 As in Figure 4.19, except for meters between 3381 and 3385-3386	4-11
4.11 As in Figure 4.19, except for meters between 3391 and 3395-3396	4-11

LIST OF FIGURES (Continued)

<u>Figure</u>		<u>Page</u>
4.12	As in Figure 4.19, except for meters between 3401 and 3404-3406	4-12
4.13	Coherence and phase between the wind stress and the shear	4-14
5.1	Auto-correlation functions of vertical shear, U-components and V-components 3393-3394	5-2
5.2	As in Figure 5.1, except for meters 3402-3403 ..	5-2
5.3	Cross-correlation functions of Horizontally separated vertical shear, U-components and V-components between 3393-3394 and 3402-3403	5-7
5.4	As in Figure 5.8, except for meters between 3394-3395 and 3403-3404	5-7
5.5	As in Figure 5.8, except for meters between 3395-3396 and 3404-3406	5-8
5.6	As in Figure 5.8, except for meters between 3395-3396 and 3385-3386	5-8
5.7	As in Figure 5.8, except for meters between 3404-3406 and 3385-3386	5-9
5.8	Cross-correlation functions of slant separated vertical shear, U-components and V-components between 3393-3394 and 3403-3404	5-10
5.9	As in Figure 5.13, except for meters between 3393-3394 and 3404-3406	5-10
5.10	As in Figure 5.13, except for meters between 3394-3395 and 3402-3403	5-11
5.11	As in Figure 5.13, except for meters between 3394-3395 and 3404-3406	5-11
5.12	As in Figure 5.13, except for meters between 3395-3396 and 3402-3403	5-12

LIST OF FIGURES (Continued)

<u>Figure</u>		<u>Page</u>
5.13	As in Figure 5.13, except for meters between 3395-3396 and 3403-3404	5-12
5.14	As in Figure 5.13, except for meters between 3385-3386 and 3393-3394	5-13
5.15	As in Figure 5.13, except for meters between 3385-3386 and 3394-3395	5-13
5.16	As in Figure 5.13, except for meters between 3385-3386 and 3402-3403	5-14
5.17	Cross-correlation functions of slant separated vertical shear, U-components and V-components between 3385-3386 and 3403-3404	5-14
5.18	Cross-correlation functions of vertically separated vertical shear, U-components and V-components between 3393-3394 and 3394-3395	5-15
5.19	As in Figure 5.23, except for meters between 3402-3403 and 3403-3404	5-15
5.20	As in Figure 5.23, except for meters between 3394-3395 and 3395-3396	5-16
5.21	As in Figure 5.23, except for meters between 3403-3404 and 3404-3406	5-16
5.22	Cross-correlation phase shifts between current meter pairs	5-18

Section 1
INTRODUCTION AND BACKGROUND

1.1 INTRODUCTION

The Ocean Measurements Program (OMP) of the Naval Ocean Research and Development Activity (NORDA) has identified the measurement and characterization of upper-ocean vertical shear as a high priority component of its mission. In support of this objective, SAI has recently completed reviews of relevant results of current research on upper-ocean vertical shear. Lambert and Patterson (1980) reviewed the measurements up through 1979, emphasizing vertical structure of currents and shear. Their summary included a discussion of the particular relevance of shear to Navy problems. Grabowski and Hebenstreit (1981) completed a comprehensive review of upper-ocean environmental models, with heavy emphasis on internal/inertial wave models.

Following these review efforts, several studies of shear were initiated. An internal-wave spectral model was used to calculate shear statistics, and an error analysis was carried out to estimate the utility of WKB scaling for extending such models into the seasonal thermocline (Grabowski, 1980). A data analysis effort focusing on vertical profiles of shear, presented some generalizations of the descriptions of the shear field for different background fields of stratification and mean currents (Patterson, et al., 1981). During the past year SAI has carried out two parallel efforts to describe upper-ocean shear. A modeling effort has emphasized modeling shear-producing dynamic

processes in the seasonal thermocline in order to aid in data interpretation and to produce models suitable for estimating shear levels under a variety of oceanographic and meteorological conditions (Rubenstein, 1981, 1982). A data analysis effort, described in this report, presents statistical descriptions of shear from an array of three current meter moorings.

Very few data sets exist which address the time-variability of upper ocean vertical shear on small scales. Two recent sets are the MILE moorings and the JASIN moorings. Another set is the one used here which we have chosen because it includes three moorings separated by several tens of kilometers, and contains relatively long time series. Although the smallest vertical separation is 20 meters, the data are particularly appropriate for characterizing the near-inertial components of shear, and provide horizontal information that the other data sets do not.

This technical report describes analyses of vertical shear time-series using data taken by the Woods Hole Oceanographic Institution between 27 June and 18 August 1970 in the vicinity of Site D ($39^{\circ}10'N$, $70^{\circ}W$). Three similar surface moorings (numbered 338, 339, and 340), spaced 50-70 km apart, were deployed in the geographical locations shown in Figure 1.1. On each mooring were a wind recorder and current meters at 12, 32, 52, and 72 m depths. Figure 1.2 shows the distribution of data in time for each current meter. The time-series from current meter 3383 was somewhat short, and 3384 returned no data. All the other time series were nearly perfect. A schematic diagram of the mooring configuration is shown in Figure 1.3, and Figure 1.4 shows the corresponding stratification profiles presented by Pollard.

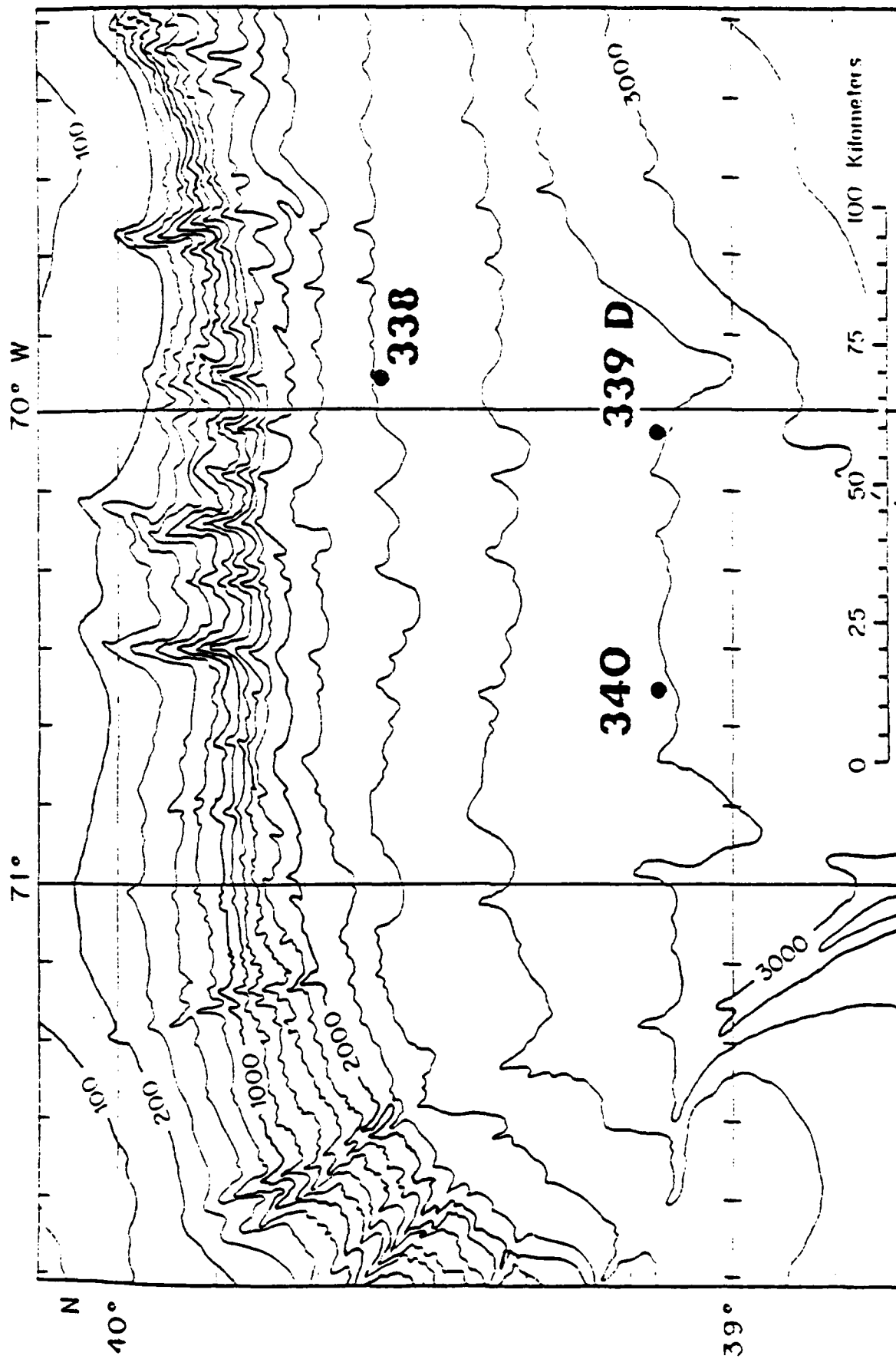


Figure 1.1: Deployment of moorings in the vicinity of Site D.

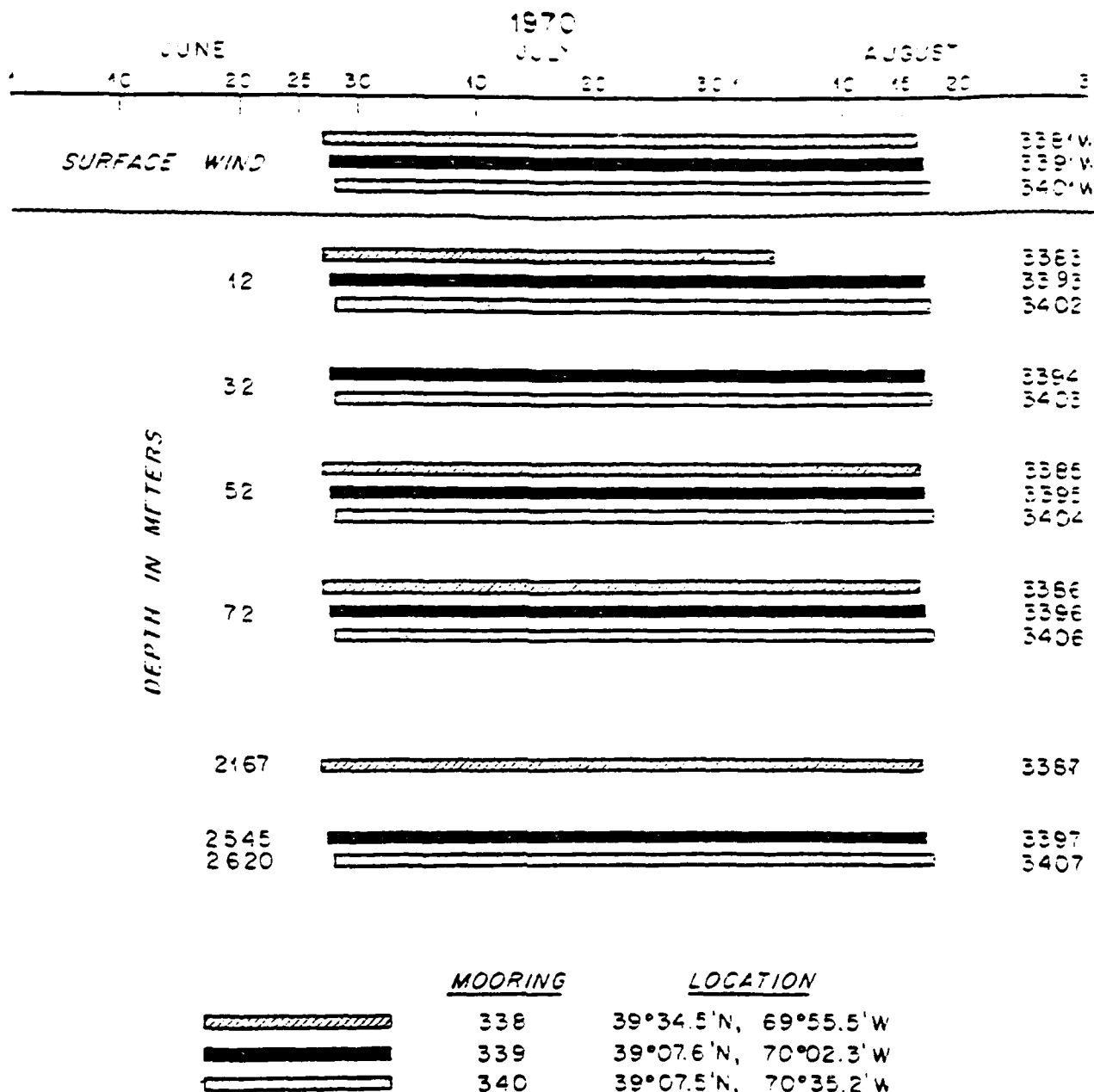


Figure 1.2: Distribution of data during Summer, 1970. The first three digits of the numbers on the right are the mooring numbers. The fourth digit indicates the sequential position of the instrument on the mooring counting from the top down.

STATION 338

5/16" 3 x 19 WIRE

9/16 NYLON,
USED

LIGHT
RADIO
WIND RECORDER - 3381

7 m CHAIN

TEMPERATURE RECORDER - 3382

CURRENT METER - 3383

18 m 3 x 19 WIRE

CURRENT METER - 3384

18 m 3 x 19 WIRE

CURRENT METER - 3385

18 m 3 x 19 WIRE

CURRENT METER - 3386

430 m

500 m

500 m

519 m

80 m

CURRENT METER - 3387

TENSIOMETER - 3388

20 m

85 m 9/16" NYLON WITH 30 GLASS
SPHERES SPACED 2 m APART

ACOUSTIC RELEASE,
TRANSPONDING

30 m 3/4" NYLON

3 m CHAIN

STIMSON ANCHOR, 3,000 LBS

Figure 1.3: Schematic diagram of mooring, from Pollard and Tarbell (1975).

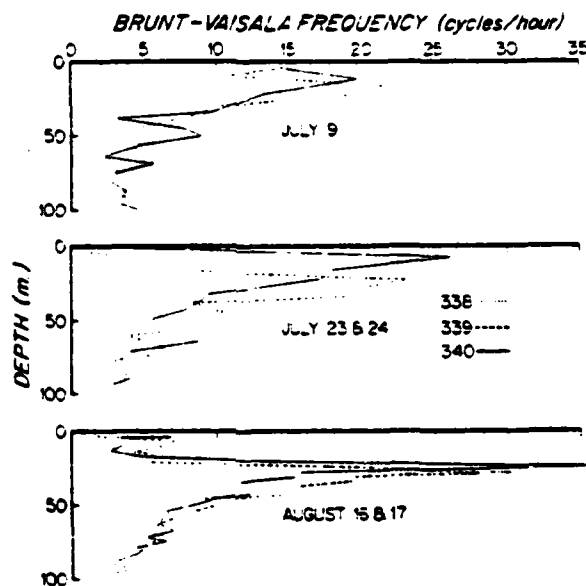


Figure 1.4: Brunt-Vaisala frequency at the three moorings on 9 and 23/24 July and 16/17 August as functions of depth in the top 100 m. The profiles were computed using averaged values of density at approximately 5 m intervals, so details of the structure particularly in the top 15 m, have been smoothed. From Pollard (1980).

1.2 BACKGROUND

Pollard (1980) examined the velocity records from these data in terms of the near-inertial frequency oscillations. He computed power spectra and coherences of velocities in the near-inertial frequency range. He found that at 12 m and 32 m, the velocities are horizontally coherent at inertial frequencies with suggested wavelengths of 700-1700 km. At 52 m and 72 m, the records were not horizontally coherent, perhaps due to differences in stratification among the mooring locations. Significant differences among the 12 m records were related to differences in local wind over the 50 km mooring spacings. Pollard found these differences could be modeled using the Pollard and Millard (1970) model with the local wind at each mooring as a forcing term. During periods of strong inertial wave generation, up to two-thirds of the energy in the mixed layer was at near inertial frequencies. Finally, the vertical component of the group velocity in the top 100 m was downward, confirming that the flow of energy was downward from the surface.

In this report we present calculations of power spectra, coherence spectra, auto-correlations, and cross-correlations from vertical shear time-series. Vertical shear is the vertical gradient of horizontal velocity. For purposes of our calculations, we approximate the shear by computing velocity differences between pairs of vertically separated time-series records.

1.3 THE GEODYNE 850 CURRENT METER

The Geodyne 850 Current Meter measures current speed using a Savonius rotor, and current direction using a

freely moving directional vane and a magnetic compass. The measurements were recorded in the "interval" mode. In this mode, bursts of rapid samples were recorded every 15 minutes. Each recording interval consisted of a burst of 20 samples at 5-second intervals, followed by a longer interval (about 800 seconds) during which no samples were taken. The currents were recorded as speed and direction. As part of the data processing, they were transferred into Cartesian coordinates, and then vector averaged to obtain a single measurement every 15 minutes.

The response of the Savonius rotor is not well understood. There is evidence that the rotor accelerates faster than it decelerates (Fofonof and Ercan, 1967), but there is also evidence of the opposite being true (see response, Halpern et al., 1981). In either case, the time constants of the rotor and directional vane are not perfectly matched.

A typical mooring (338) is shown schematically in Figure 1.3. The other two moorings were similar, especially the upper four current meters with which we are concerned. The toroidal surface buoys support a metal triangular pyramid superstructure. Within this superstructure is placed the wind recorder. In order to prevent an upwind superstructure strut from creating spurious effects, a large plywood fin is attached to one of the struts. This helps to orient the buoy so that the wind impinges on the wind sensor midway between two struts.

Halpern et al. (1981) performed tests to determine the effects of mooring motions on current meter measurements. He compared the spectra from upper ocean (above

100 m) current meters supported by surface buoys with current meters supported by spar and subsurface buoys. He defined a quantity called the "maximum usable frequency", the frequency threshold above which the power spectra from two current meters (at the same depth but attached to different moorings) diverge. In the upper 30 m, the maximum usable frequency was at least 2 cph in all cases. In the depth range 79-94 m, where the currents were much weaker, the maximum usable frequency fell in the range 0.2-2 cph. As we are interested in shear near the inertial frequency, 0.053 cph, this limitation is of little consequence.

Section 2
STATISTICS PROCEDURES

2.1 POWER SPECTRAL DENSITIES

Calculations of power spectral densities follow the procedure outlined below.

1. Select a length of record with a number of data points M equal to a power of two.
2. The data record is multiplied by a Hanning window function

$$w_{T/2}(t) = \frac{1}{2} A(1 + \cos 2\pi t/T),$$

where t is time, T is the total length of the record, and the scale factor $A = \sqrt{8/3}$ insures that the variance remains unchanged. The corresponding filter $W(f)$ is given by the Fourier transform of $w_{T/2}(t)$;

$$W(f) = \frac{\sin \pi f T}{2\pi f} (1 - f^2 T^2)^{-1}.$$

Figure 2.1 shows the shape of $W(f)$, for the particular case $T = 1$.

3. The fast Fourier transform of the u -component is computed as follows:

$$U_k = \text{FFT}(u_m) = \sum_{m=0}^{M-1} u_m \exp(-i \frac{2\pi km}{M})$$

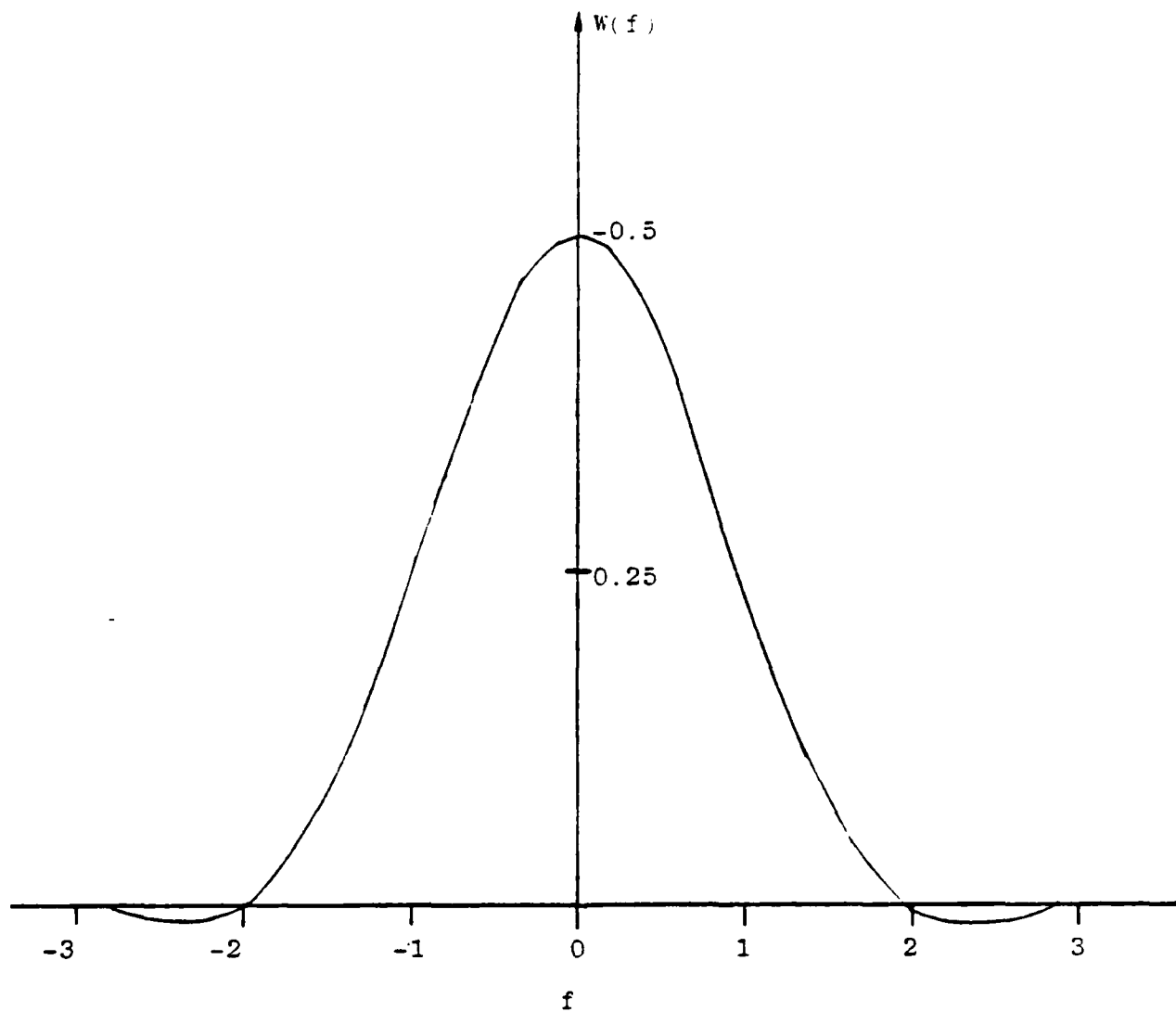


Figure 2.1 Frequency response $W(f)$
for a Hanning window function.

where

U_k = kth spectral coefficient

u_m = mth u-component of velocity

and the v-component is computed similarly.

4. Raw spectral estimates are computed;

$$S_k = \frac{2\Delta t}{M} (|U_k|^2 + |V_k|^2)$$

corresponding to frequencies

$$f_k = \frac{k}{\Delta t M} ; k = 0, 1, \dots, M/2-1.$$

5. Band averaging is performed, providing 50 smoothed spectral estimates. The number of raw estimates used to compute the smoothed spectrum varies from 2 in the lowest bins up to 347 in the highest bin. The distribution of smoothed estimates is designed to keep the values of $\log f_k$ nearly evenly spaced, and to resolve the inertial and semi-diurnal frequencies. In the bin containing the inertial frequencies, 7 raw estimates are averaged.

6. The smoothed spectral estimates are multiplied by frequency f , and plotted on a linear scale versus $\log f$. This format, often called a variance-preserving plot, provides constant variance per unit area under the curve. Frequency bands which contribute significantly to the total variance are easily recognized by this method.

2.2 VECTOR COHERENCE SPECTRAL FUNCTIONS

We follow the procedure outlined by Gonella (1972) for computing the vector coherence functions. This procedure is equivalent to that described below.

1. Begin with two discrete vector time series, in complex form;

$$\begin{aligned}\underline{u}_1(t_m) &= u_1(t_m) + iv_1(t_m), \\ \underline{u}_2(t_m) &= u_2(t_m) + iv_2(t_m); \\ m &= 0, 1, \dots, L-1.\end{aligned}$$

The integer L is chosen to be an integer (I) multiple of J , where J is a power of two;

$$L = IJ.$$

Divide each of the two time series into $2I-1$ short series, overlapping one another by 50%, and each of length J .

2. Multiply each of the short series by a Hanning window function, described in the previous section.

3. The two-sided Fourier transform (the transform is not symmetric with respect to zero frequency) is computed for each short complex series;

$$\begin{aligned}\underline{U}_1(f_k) &= \sum_{m=0}^{M-1} \underline{u}_1(t_m) \exp(-i \frac{2\pi km}{M}), \\ k &= -M/2, \dots, (M/2)-1,\end{aligned}$$

and similarly for $\underline{U}_2(f_k)$.

4. The auto, coincident, and quadrature spectral density functions P and Q are computed:

$$P_{11}(f_k) = \langle \underline{U}_1(f_k) \underline{U}_1^*(f_k) \rangle$$

$$P_{22}(f_k) = \langle \underline{U}_2(f_k) \underline{U}_2^*(f_k) \rangle$$

$$P_{12}(f_k) - iQ_{12}(f_k) = \langle \underline{U}_1(f_k) \underline{U}_2^*(f_k) \rangle$$

where the asterisk denotes a complex conjugate, and the brackets denote ensemble averages over the $2L - 1$ ensembles. This procedure provides estimates with $2L$ degrees of freedom.

5. Compute the coherence amplitude and phase, defined by

$$C(f_k) = \left[\frac{P_{12}^2 + Q_{12}^2}{P_{11}P_{22}} \right]^{1/2},$$

$$\phi(f_k) = \arctan(Q_{12}/P_{12}).$$

for frequencies $f_k = k/(N\Delta t)$, for $k = -M/2, \dots, M/2-1$. Negative frequencies indicate clockwise rotation and positive frequencies indicate counterclockwise rotation.

2.3 NORMALIZED CORRELATION FUNCTIONS

Normalized auto-correlation and cross-correlation functions are computed following the procedure outlined below.

1. A maximum lag g is chosen.

2. Normalized correlation is computed:

$$C_{xy}(r\Delta t) = \frac{\sum_{m=1}^{M-g} (x_{m+r} - \bar{x})(y_m - \bar{y})}{\left[\sum_{m=1}^{M-g} (x_m - \bar{x})^2 \sum_{m=1}^{M-g} (y_m - \bar{y})^2 \right]^{1/2}}$$

$$r = -g, \dots, g.$$

The overbars denote mean values.

Section 3 POWER SPECTRA

In this section we discuss power spectra of the velocity and shear (velocity difference) time series. The method of computing power spectra is described in Section 2. Our purpose is to examine the relative contributions by individual frequency bands. It is convenient to categorize these bands according to the physical processes with which they are associated. We divide the frequency domain into four bands: low frequency, near-inertial, semidiurnal and internal wave. In Section 3.1 we present a brief background review of the physical processes that generate kinetic energy in these frequency bands. In Section 3.2 we discuss the velocity spectra computed by Pollard (1980). In Section 3.3 we present and discuss spectra of the shear between various pairs of current meters.

3.1 FORCING MECHANISMS

3.1.1 Near-Inertial Oscillations

We shall see that the near-inertial frequency band is generally a strong contributor to the total shear variance in upper ocean power spectra. The inertial frequency f is defined as twice the magnitude of the projection of the earth's angular rotation vector on the local vertical unit vector (i.e., $f = 2\Omega \sin \lambda$, where Ω is the earth's angular rotation rate, and λ is the latitude). At the latitude of Pollard's current measurements ($\lambda = 40^\circ$), the inertial frequency is $f = 9.3 \times 10^{-5} \text{ rad/sec}$ or .053 cycles/hr.

The inertial frequency is the natural frequency of oscillation in a rotating unstratified fluid. When a sudden change in the wind stress is applied over the ocean, the horizontal currents in the upper ocean are deflected in the clockwise sense (in the Northern Hemisphere) by the Coriolis force. The velocity vector begins rotating in the clockwise direction. These oscillations are often observed in the upper ocean, for several days after the passage of an atmospheric front.

3.1.2 Semi-Diurnal Oscillations

The oscillations observed at the semi-diurnal frequency are tidal currents. Regal and Wunsch (1973) describe observations of internal tides at several upper ocean stations, including Site D. At this site, most of the semidiurnal energy is in baroclinic modes, and is classified as the lunar (M_2) constituent, with a period of 12.42 hours. Regal and Wunsch explain that the baroclinic tidal component is predominant here because of the interaction of tidal motions with the geometry of the nearby edge of the continental shelf. Internal tides are generated at the sharp break in the bottom slope, just to the north of Site D. As shown in Figure 3.1, internal wave energy propagates along characteristic lines given by $z + cy = \text{constant}$, where z is vertical, y is horizontal, and $c^2 = (\omega^2 - f^2) / (N^2(z) - \omega^2)$. One of the internal wave characteristics, represented by the solid line labeled A, lies nearly tangent to the continental slope, and reaches Site D after a single bounce. Regal and Wunsch suggest, without detailed explanation, that internal wave energy is focused at the surface near the site. Other characteristics also arrive near Site D, but the focusing effect is not as pronounced.

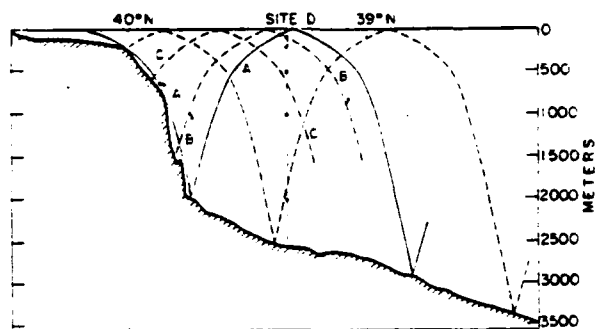


Figure 3.1: Profile of relief along 70°W (see Figure 1.1 for local isobaths) together with selected semidiurnal period internal wave characteristics passing near site D. Note the solid characteristic line (labeled A) which is nearly tangent to the continental slope and reaches site D in a single bounce. (Regal and Wunsch, 1973)

3.1.3 Low Frequency Motions

We have partitioned the low frequency band as $\omega < f$ because it represents motions caused by several different physical processes excluding internal waves. Internal waves cannot propagate freely at frequencies less than the local inertial frequency. Low frequency motions have a variety of generating mechanisms. Among these mechanisms are slow changes in the large-scale wind stress and changes in the ocean's baroclinic density structure. We will not further describe these processes in this report. Our shear spectra generally do not show much energy in the low frequency bands.

3.1.4 Internal Wave Band

A large number of mechanisms have been advanced for the generation of internal waves. We touch upon just a few of the most likely mechanisms here. The variability of internal-wave energy in the upper ocean suggests that some mode of surface forcing may be important. Surface forcing by traveling fluctuations of divergent wind stress induces vertical motions at the bottom of the surface boundary layer. Traveling fluctuations in buoyancy flux give rise to pressure fluctuations which also induce vertical motions at the base of the surface layer. These motions generate internal waves which are free to propagate into the interior (Thorpe, 1975). Internal waves may be induced by currents flowing over bottom topography. We have already discussed, in Section 3.1.2, the possibility of internal waves being generated by tidal motions through the latter mechanism.

In this report we propose yet another possible mechanism for the generation of some portion of the kinetic

energy in the internal wave band. Under certain conditions, strong inertial oscillations may interact nonlinearly with the strong tidal component. Energy at the difference frequency, being smaller than f , cannot propagate, but energy at the sum of the inertial and semidiurnal frequencies can propagate as a free internal wave into the stratified interior. Our spectra show evidence of a component at this frequency. Krauss (1981) observed a similar spectral component in the Baltic Sea at twice the inertial frequency.

3.2 VELOCITY SPECTRA

Figure 3.2 shows the velocity spectra computed by Pollard (1980). Two peaks at the inertial and semidiurnal frequencies are the most prominent features in these spectra. At the two shallowest depths, 12 and 32 m, the inertial peak is stronger relative to the semidiurnal peak. At 52 and 72 m, the opposite is the case. Note that the vertical scales of the plots are different at each depth.

The semidiurnal peak is most energetic at all depths at moorings 339 and 340. As discussed in Section 3.1.2, this may be due to their position relative to the continental slope. Conditions are such that moorings 339 and 340 are in the most favorable location to receive the benefits of the internal tides focusing effect.

In the mixed layer, at 12 m, the inertial peaks recorded at the three moorings were of comparable magnitude. At 32, 52, and 72 m, mooring 340 shows the strongest inertial oscillations. Pollard (1980) showed that two fronts passed each of the current meter arrays on 11 August, and that during this period current meter 3383 was not in

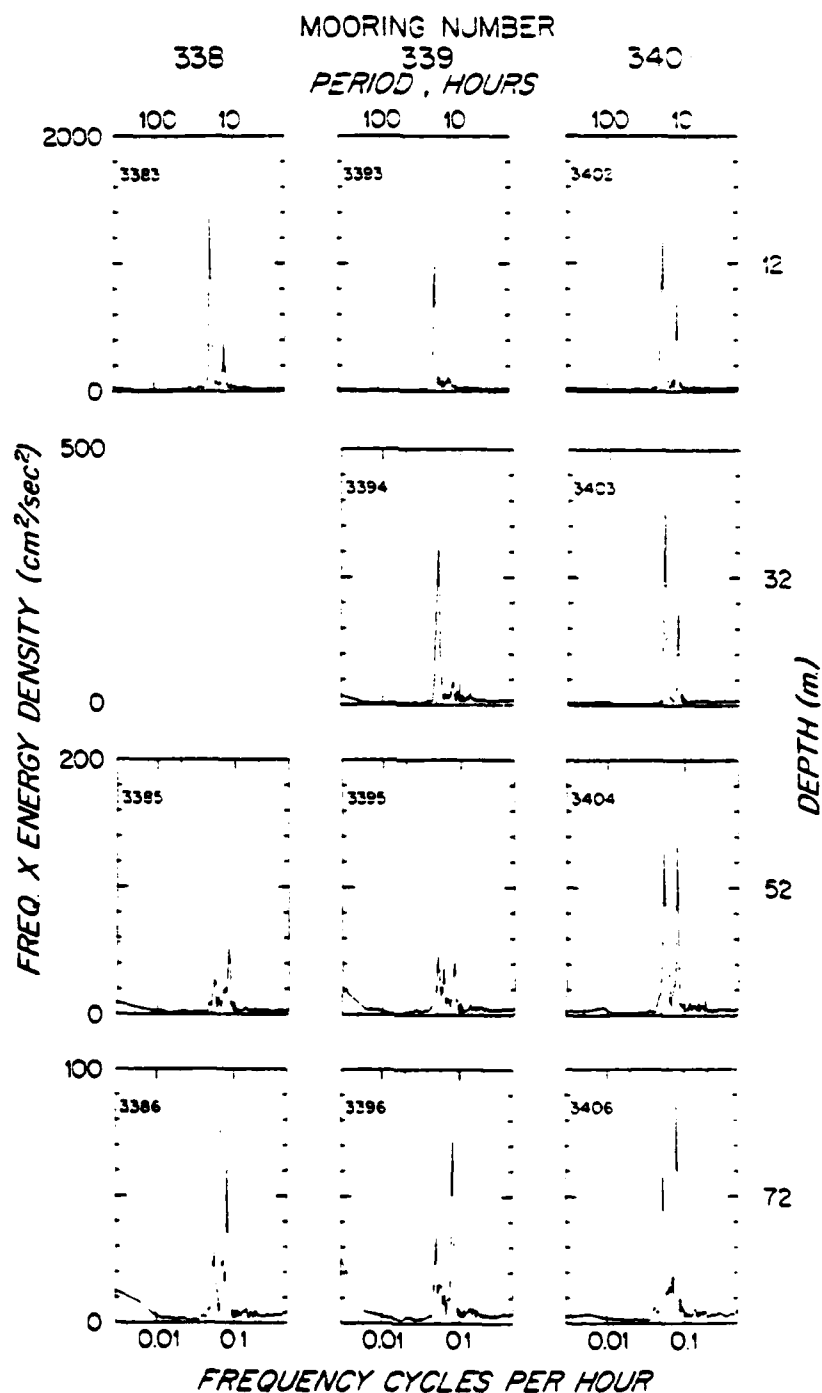


Figure 3.2: Spectra of all records in the top 100 m using 1024 h of data between 28 June and 10 August. The abscissa is log-frequency on the lower scale, log-period on the upper scale of each plot. The ordinate is the energy density, scaled by the frequency, plotted linearly. Note that the energy scale is different at different depths, but the same for all records at a fixed depth. The area under this plot in any given frequency band is proportional to the energy in that band. Dominant peaks are inertial (18.78 h) and tidal (12.42 h). From Pollard (1980).

operation. The time difference between arrival of the fronts at 340, 338, and 339 were 7, 12, and 16 hours, respectively. As a result, the inertial amplitudes after the passage of the fronts were observed to be much stronger at 340 than at 339. At 339, energy input by the wind during the first half of an inertial period is subtracted during the second half. Thus, the energy at the inertial frequency appears to be quite sensitive to small differences in the wind stress.

The relative contributions by the low frequency and internal wave bands are practically negligible at 12 and 32 m. At 52 and 72 m, the relative contributions in these frequency bands are somewhat greater.

3.3 SHEAR SPECTRA

3.3.1 Results

Power spectral density was computed for the velocity differences between pairs of vertically adjacent current meters. Since the interval between data samples was 15 minutes, the Nyquist frequency was 2 cycles per hour. Since the fast Fourier transform algorithm requires the record length to be a power of two, the record length was chosen to contain 4096 samples. The data were not filtered prior to the computation of spectral estimates. Table 3.1 lists the current meter pairs for which spectra were computed, along with their respective depths. The spectral density functions are displayed in variance-preserving format in Figures 3.3 through 3.9. Velocity differences between non-adjacent current meters were not analyzed because these differences are dominated by the relatively large velocities at the upper current meter. Analysis of these velocity

TABLE 3.1

POWER SPECTRA OF VELOCITY DIFFERENCES
(VERTICAL SHEAR)

<u>Fig.</u>	<u>Current Meters</u>	<u>Depths (m)</u>
3.3	3393-3394	12-32
3.4	3402-3403	12-32
3.5	3394-3395	32-52
3.6	3403-3404	32-52
3.7	3385-3386	52-72
3.8	3395-3396	52-72
3.9	3404-3406	52-72

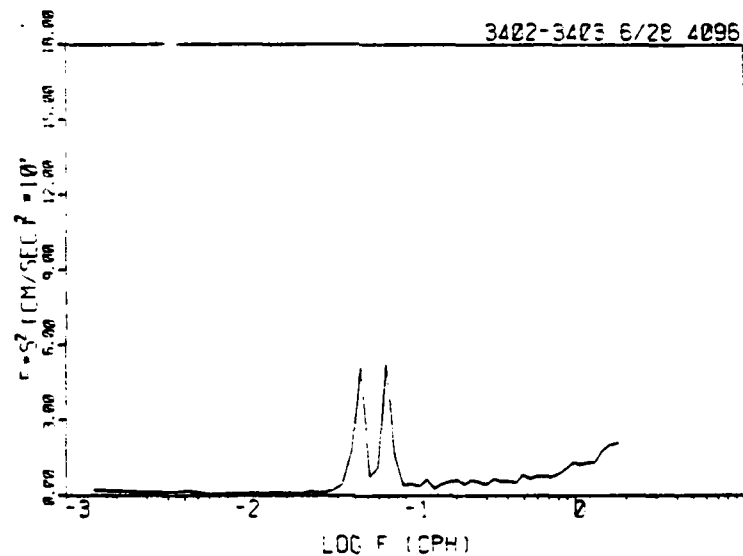
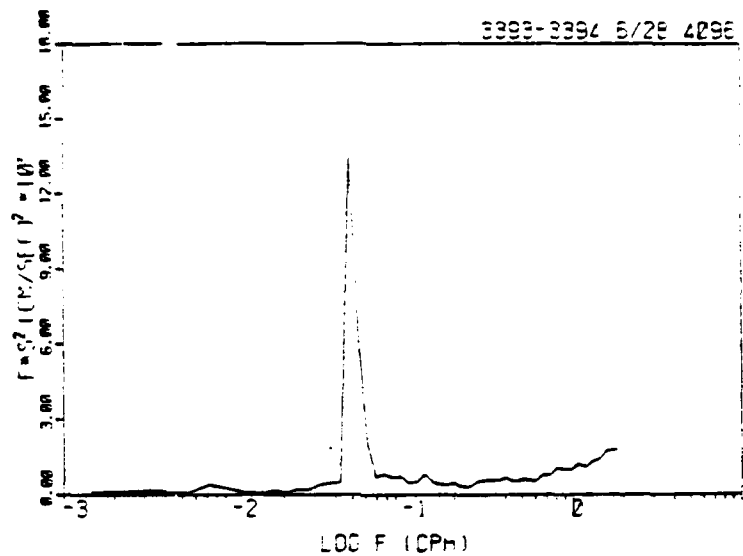


Figure 3.3: (Top) Power spectrum of vertical shear, current meters 3393-3394, at depths 12 and 32 m, respectively.

Figure 3.4: (Bottom) As in Figure 3.3, except for meters 3402-3403.

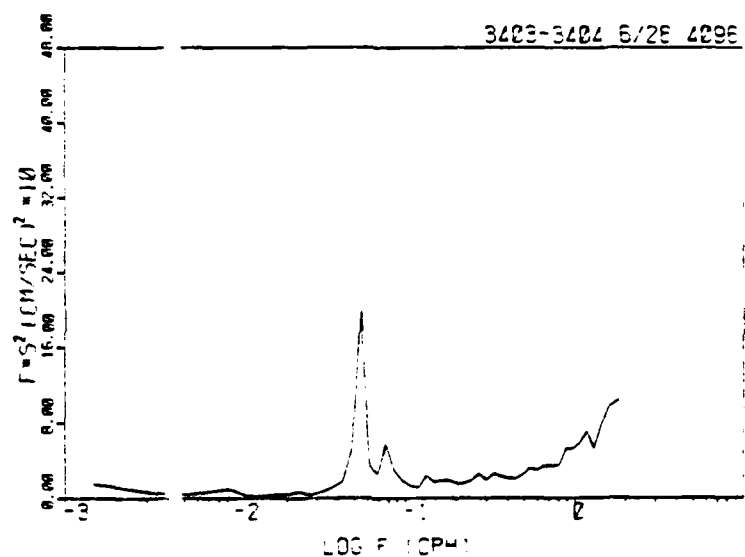
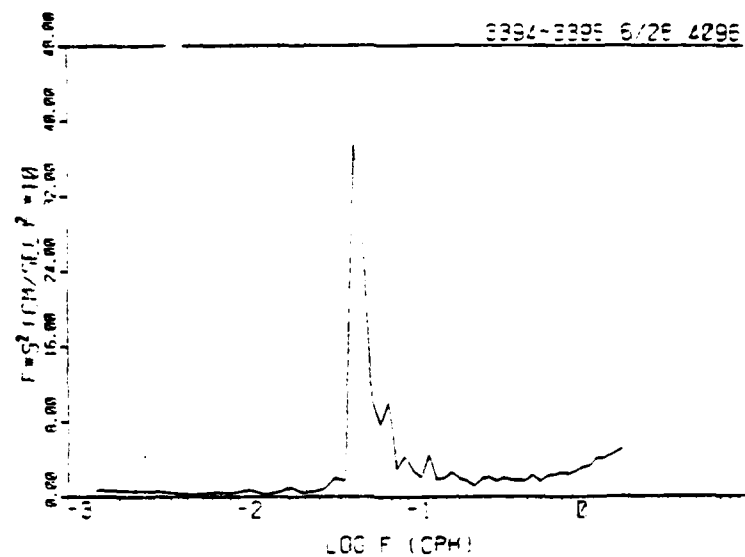


Figure 3.5: (Top) Power spectrum of vertical shear, current meters 3394-3395, at depths 32 and 52 m, respectively.

Figure 3.6: (Bottom) As in Figure 3.5, except for meters 3403-3404.

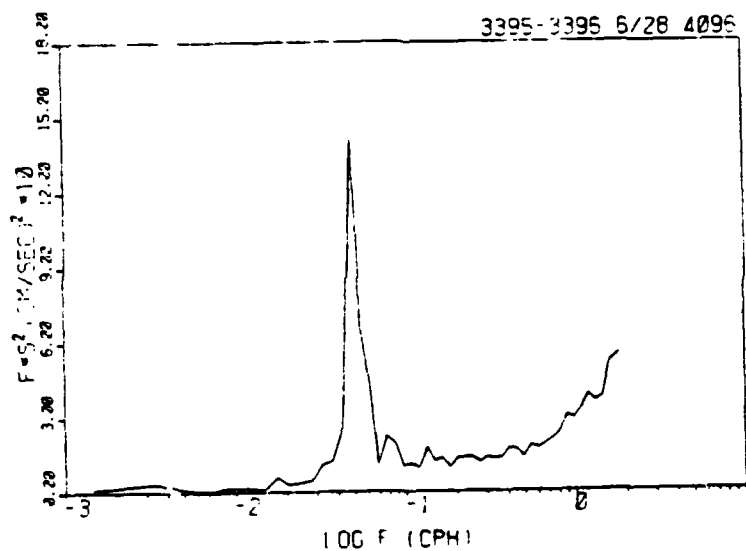
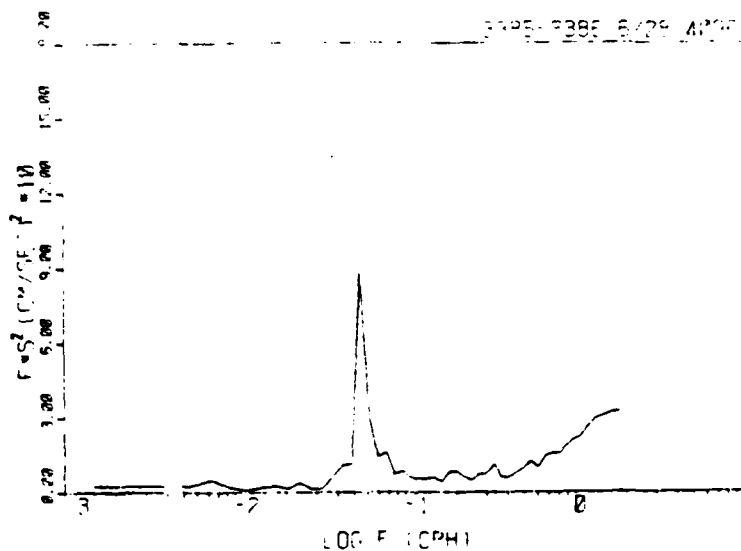


Figure 3.7: (Top) Power spectrum of vertical shear, current meters 3385-3386, at depths 52 and 72 m, respectively.

Figure 3.8: (Bottom) As in Figure 3.7, except for meters 3395-3396.

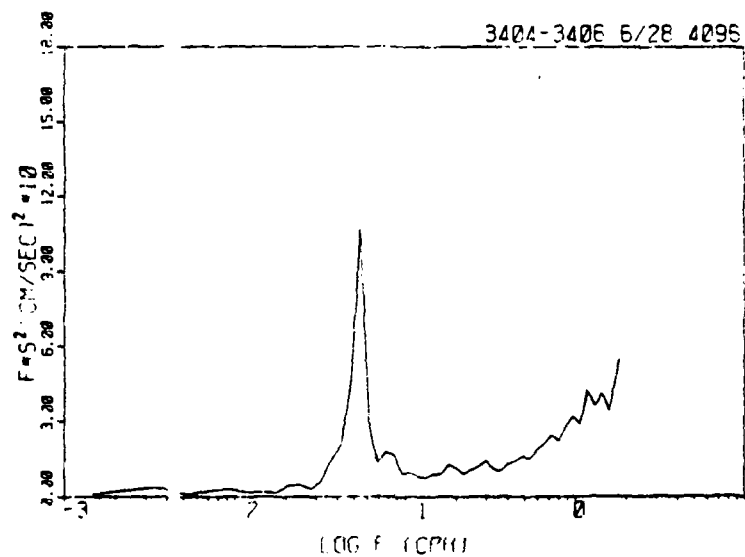


Figure 3.9: As in Figure 3.7. except for meters 3404-3406.

differences would therefore be nearly equivalent to the analysis of individual current meter records previously done by Pollard (1980).

The spectra in Figures 3.3 - 3.9 are for horizontal velocity differences over $\Delta z = 20$ m vertical separation. We can convert these to shear spectra simply by dividing by Δz^2 . Grabowski and Newman (1981) used a vertical wavenumber shear spectral model based on that compiled by Gargett et al. (1981), to determine the dependence of mean square shear on Δz . Grabowski and Newman found that mean square shear varies as Δz^{-1} . Therefore, much of the small vertical-scale shear variance is missed due to the large (20 m) vertical separation of the current meters. Extending the results in Table 1 of Grabowski and Newman, the shear variance observed with a vertical sample interval $\Delta z = 20$ m is 54% of the variance observed with $\Delta z = 10$ m and 14% of the variance observed with $\Delta z = 2$ m.

3.3.2 Inertial and Tidal Shear

Sharp peaks are evident in all of the spectra at the inertial frequency, .053 cph. The peaks are strongest at the shallowest depth pair (12 - 32 m), and decrease in magnitude with depth. As was the case for the velocity spectra, the inertial band energy varies from one mooring to the next, because the shear response is sensitive to small differences in the wind stress.

The inertial peak in each (20 m velocity difference) shear spectrum is comparable in magnitude to the peak in the velocity spectrum of the corresponding upper current meter. The reason is that the inertial oscillations decay rapidly with depth. The 20 m velocity differences are

therefore dominated by the velocities recorded by the upper current meters.

Distinct peaks at the semidiurnal frequency are present in most of the shear spectra, but only in Figure 3.4 is the peak comparable to the inertial peak. This result is in contrast with the velocity spectra, which show strong peaks of magnitude comparable to the inertial peaks for about half of the records. The implication is that, even if the tidal oscillations are baroclinic, their vertical wavelengths are generally much greater than 20 m.

3.3.3 Aliasing in the Internal Wave Band

The spectral levels of vertical shear increase with frequency from 0.5 - 2.0 cph in the internal wave band. In Pollard's velocity spectra (Figure 3.2) this increase is not apparent because the spectra were terminated at 0.5 cph. This increase may be a contaminating effect of mooring motion, an aliasing effect, or some combination of both. Halpern et al. (1981) discuss intercomparison tests between current measurements in the upper ocean made with different types of current meters and moorings. They find that VACM (Vector Averaging Current Meter) measurements are more susceptible to spurious mooring motions in the seasonal thermocline (below 50 m) than in the mixed layer where the current magnitudes are stronger. In comparisons between VACM measurements taken from moorings attached to surface and subsurface buoys, the surface buoy data are more noisy. Halpern et al. define a "maximum usable frequency" as the frequency above which two compared spectra begin to diverge. In the mixed layer, the maximum usable frequency is about 4 cycles per hour. In the seasonal thermocline (79 m) the maximum usable frequency ranges from about 0.2 to 2 cycles per hour.

In the present data set, the current meters recorded data at the rate of 4 samples per hour. It is possible that the data were under-sampled; energy at higher frequencies may be aliased, or folded into the computed spectra. We cannot judge the degree of aliasing from these spectra alone. However, we can show an example of how aliasing affects a model spectrum. Figure 3.10 shows a portion of a spectrum of horizontal velocity, based on the Garrett and Munk model (Munk, 1981). The spectrum is shown in variance preserving form--variance in a given frequency band is proportional to the area under the curve. It is based upon an inertial frequency $f = 0.053$ cph and a local Vaisala frequency $N = 4$ cph. If the current meter sampling rate is 4 samples per hour, then the Nyquist frequency is 2 cph. Power in the frequency band between 2 and 4 cph is aliased into the computed spectrum. The aliased spectrum overestimates the spectral magnitude, especially between 1 and 2 cph.

3.3.4 Dissipation of Inertial Oscillations

One of the biggest problems in our understanding of inertial oscillations is the mechanism by which they are dissipated in the upper ocean. Several mechanisms have been suggested, but none of these prove to be wholly satisfactory.

Pollard (1980) estimates that in the mixed layer, the inertial oscillations during the period 30 June - 5 July decreased in amplitude from 40 cm s^{-1} to 20 cm s^{-1} . This corresponds to an energy loss rate of $4 \text{ ergs cm}^{-2} \text{ s}^{-1}$. He derives a simple estimate of the energy loss rate due to simple dispersion of near-inertial internal waves, approximately $0.5\text{-}1.5 \text{ erg cm}^{-2} \text{ s}^{-1}$. This discrepancy shows that dispersion alone cannot account for the energy loss.

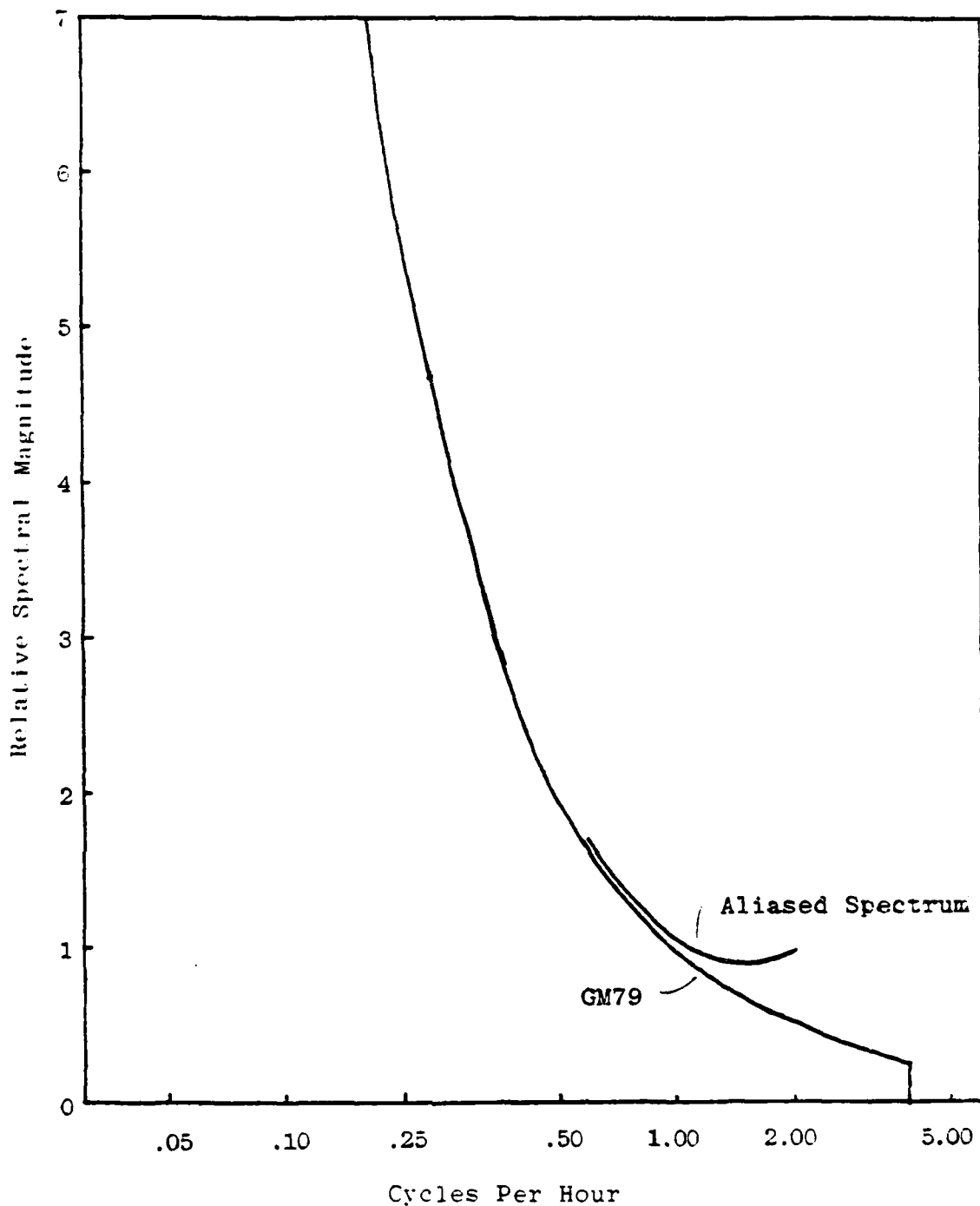


Figure 3.10: Garrett and Munk horizontal velocity spectral model, (GM79) frequency dependence $F_U(\omega) \propto (\omega^2 + f^2)\omega^{-3}(\omega^2 - f^2)^{-\frac{1}{2}}$, in variance preserving form. Inertial frequency is $f = .053$ cph, Vaisala frequency is $N = 4$ cph. Also, if data are under-sampled at a rate of 4 samples per hour, the spectrum is aliased as shown.

The generation time scale of inertial oscillations (~ 1 day) is much shorter than the dissipation time scale (~ 5 days). This fact helps to explain why the oscillations are concentrated in the surface layer. Widely spaced wind events quickly stir up inertial motions, which take many days to dissipate.

Other mechanisms for the dissipation of inertial energy have been advanced. Pollard et al. (1973) suggest the possibility that the Kelvin-Helmholtz instability at the mixed layer base may remove energy from the inertial oscillations. This suggestion is supported by observations and numerical computations of small Richardson number at the mixed layer base by Krauss (1981). Bell (1978) suggests that turbulence-induced undulations in the mixed layer-thermocline interface may be advected by inertial oscillations. These undulations are forced to do work against the underlying stratified fluid, and may generate radiation-damping internal waves.

Our shear spectra suggest that another mechanism may also be at work. There are small elevations in the spectral levels at the frequency ~ 0.13 cph, the sum of the inertial and semidiurnal frequencies. Their consistent appearance in most of the spectra is suggestive of a nonlinear resonant interaction taking place. If a nonlinear interaction is sufficiently strong, then energy at the sum and difference frequencies $f \pm \omega_s$, (where ω_s is the semidiurnal frequency) is generated. Energy at the difference frequency, being smaller than f , is not free to propagate. Energy at the sum frequency is free to propagate into the stratified interior. As the angle of propagation of this internal wave component is steeper than the near-inertial

component, its vertical group velocity is greater and hence, its energy dispersion rate may also be greater. Observations by Krauss (1981) in the Baltic Sea show spectral peaks at $2f$. A similar resonant nonlinear interaction may be occurring there, and may be further evidence for such a radiation damping mechanism.

Section 4

COHERENCE SPECTRA

Coherence spectral functions were computed between pairs of vertical shear measurements (velocity differences), separated horizontally and vertically. Coherence and phase spectra were also computed between wind stress and vertical shear time series. Section 2 described the procedure used to compute vector coherence and phase.

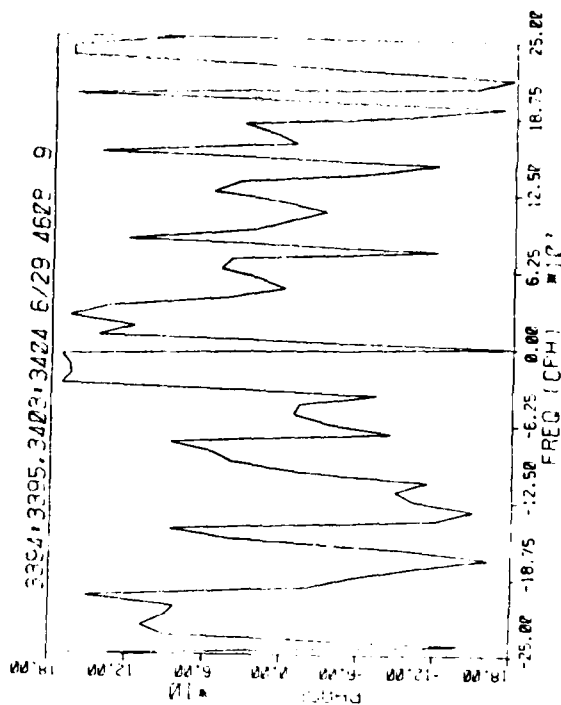
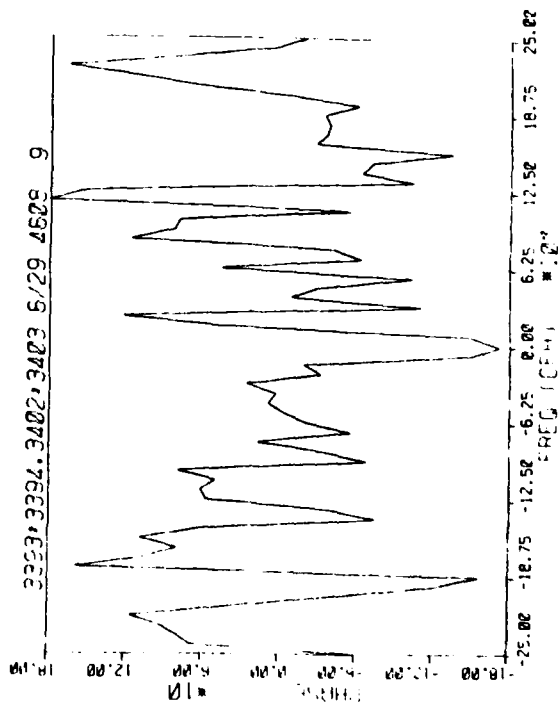
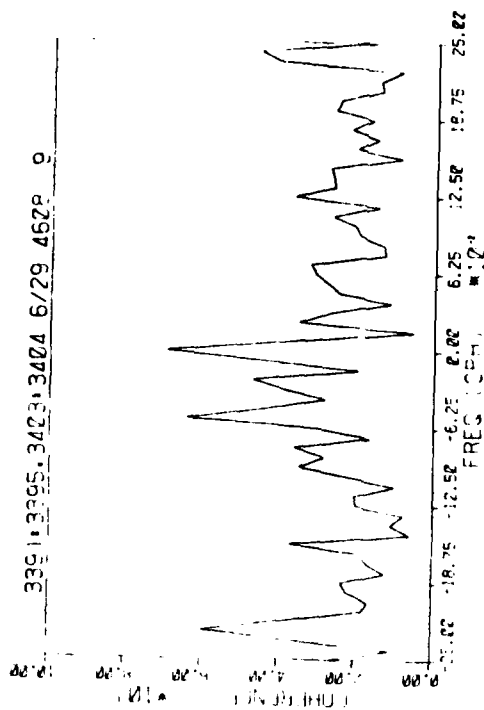
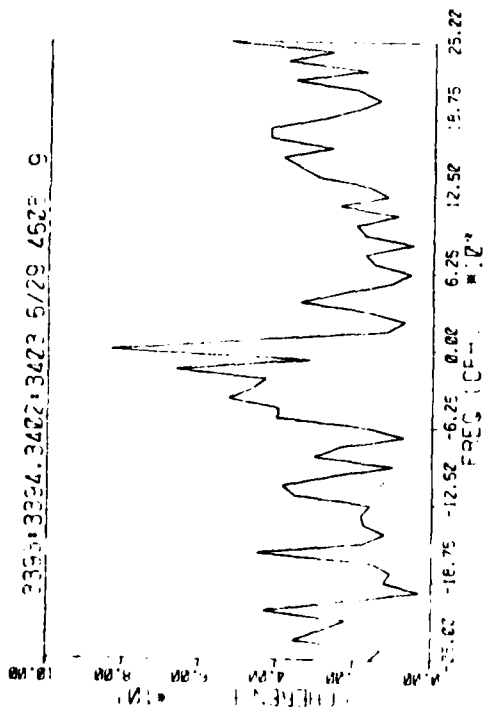
4.1 HORIZONTAL COHERENCES

Following the notation of Section 2, all coherence computations were based on records of length, $L = 4608$. In the horizontal and slant coherences, and in the wind stress/shear coherence calculations, most of the significant coherence was in the frequency range $(-.25, .25)$ cph. Here negative frequencies indicate clockwise rotation, positive frequencies indicate counterclockwise rotation. In order to provide sufficient resolution in this frequency range, M was chosen to be 9, giving 17 overlapping series, each of length $J = 512$. This choice allowed $2M = 18$ degrees of freedom. The 90% confidence level was 0.53.

Horizontal coherence amplitude and phase functions were computed between vertical shear (velocity difference) time series. Table 4.1 conveniently lists the figures, with their respective current meter numbers, depths, and approximate horizontal separations. The coherence spectra are displayed in Figures 4.1 through 4.5. The frequency range of

TABLE 4.1
COHERENCE SPECTRA BETWEEN HORIZONTALLY
SEPARATED VERTICAL SHEAR MEASUREMENTS

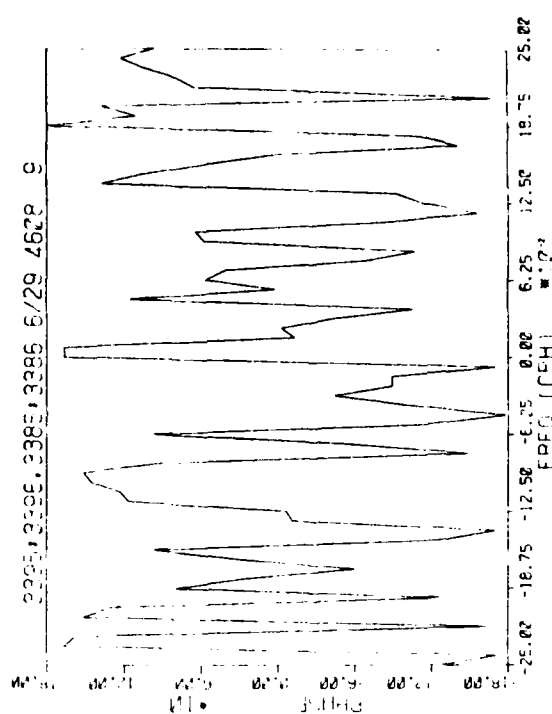
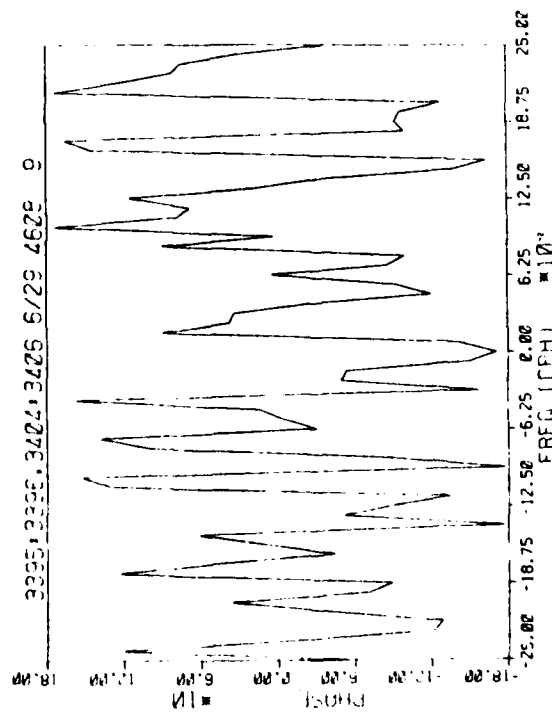
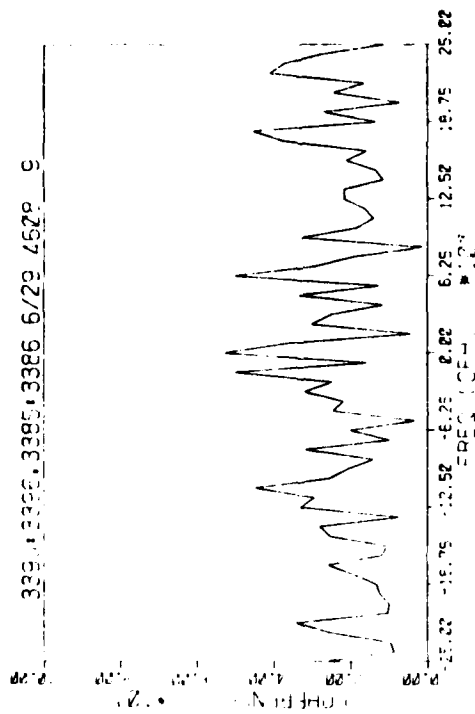
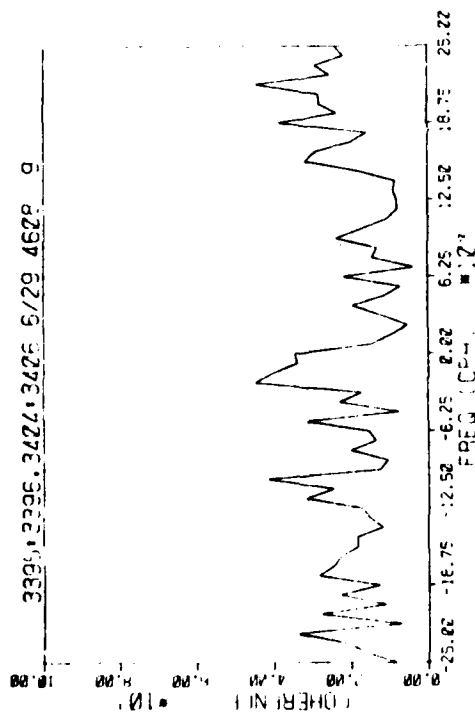
<u>Fig.</u>	<u>Current Meters</u>	<u>Depth (m)</u>	<u>Approximate Horizontal Separation (km)</u>
4.1	3393-3394/3402-3403	12-32	47
4.2	3394-3395/3403-3404	32-52	47
4.3	3395-3396/3404-3406	52-72	47
4.3	3395-3396/3385-3386	52-72	51
4.5	3404-3406/3385-3386	52-72	69



Horizontally Separated Vertical Shear Coherence Amplitudes (Top) and Phases (Bottom).

Figure 4.1 (Left): Between 3393-3394 and 3402-3403.

Figure 4.2 (Right): Between 3394-3395 and 3403-3404.



Horizontally Separated Vertical Shear Coherence Amplitudes (Top) and Phases (Bottom).

Figure 4.3 (Left): Between 3395-3396 and 3404-3406.

Figure 4.4 (Right): Between 3395-3396 and 3385-3386.

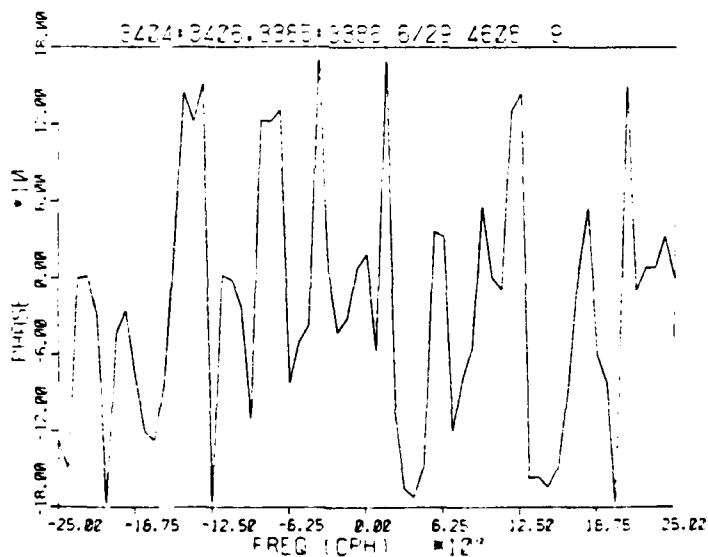
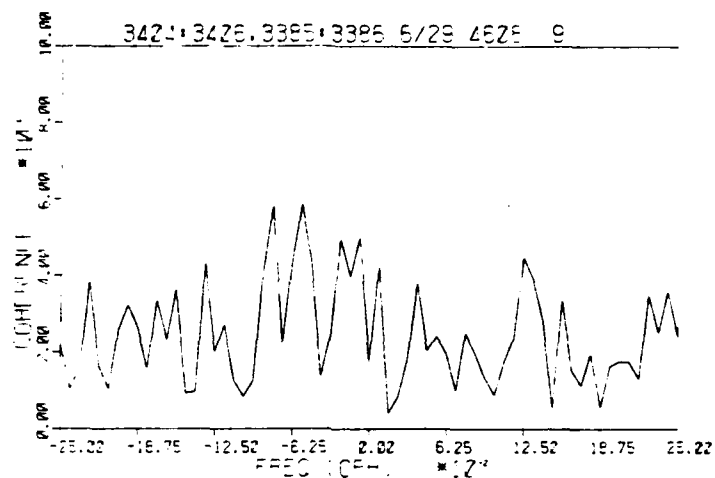


Figure 4.5 Horizontally Separated Vertical Shear Coherence Amplitude (Top) and Phase (Bottom), Between 3404-3406 and 3385-3386.

display is between -0.25 to 0.25 cph. In Figures 4.1 and 4.2, the coherence amplitude is strong in the frequency range $(-f, 0)$. This result is similar to Gonella's (1972) finding that the coherence between horizontally separated near-surface current measurements was strong in this range. For deeper shear measurements, the coherence amplitude (Figures 4.3 through 4.5) is also significant at some frequencies in this range, but it is not as strong as for the near-surface measurements.

4.2 VERTICAL COHERENCES

Vertical rotary coherence spectra of shear time series were computed, but showed rather anomalous results. For example, some rotary spectra of vertically adjacent time series exhibit a minimum in coherence at the inertial frequency. These calculations and their interpretation require further study.

4.3 WIND STRESS/SHEAR COHERENCES

Coherence amplitude and phase functions were computed between wind stress and vertical shear time series. Table 4.2 lists the wind recorders and current meters used in the coherence calculations.

Wind stress $\underline{\tau}$ was computed from the drag law

$$\underline{\tau} = \rho C \underline{U} |\underline{U}|,$$

where ρ is the air density, and \underline{U} is the mean wind velocity vector, with magnitude $|\underline{U}|$. The stress coefficient C was

TABLE 4.2
COHERENCE SPECTRA BETWEEN WIND STRESS
AND VERTICAL SHEAR MEASUREMENTS

<u>Fig.</u>	<u>Wind Recorder/Current Meters</u>	<u>Depth (m)</u>
4.6	3391/3393-3394	12-32
4.7	3401/3402-3403	12-32
4.8	3391/3394-3395	32-52
4.9	3401/3403-3404	32-52
4.10	3381/3385-3386	52-72
4.11	3391/3395-3396	52-72
4.12	3401/3404-3406	52-72

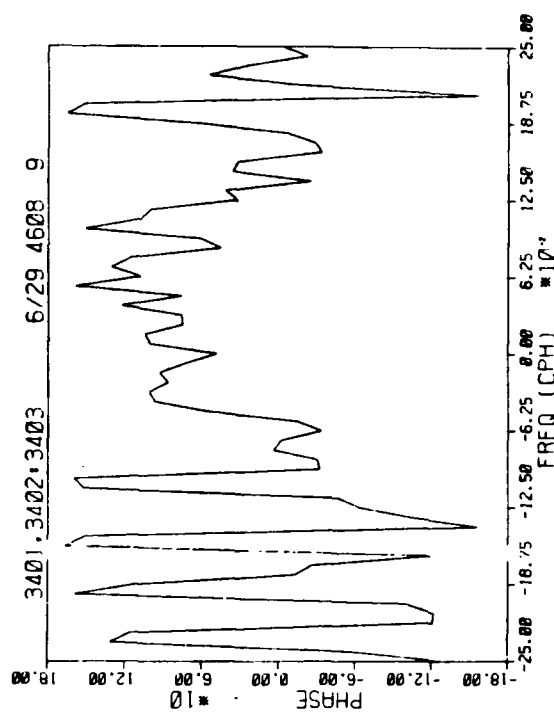
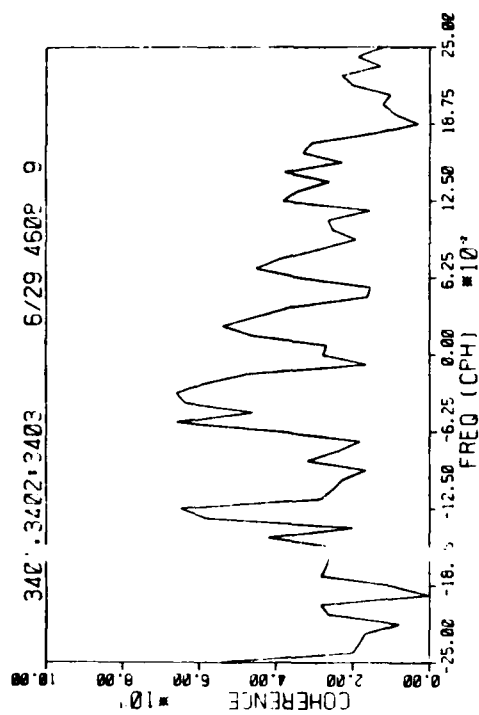
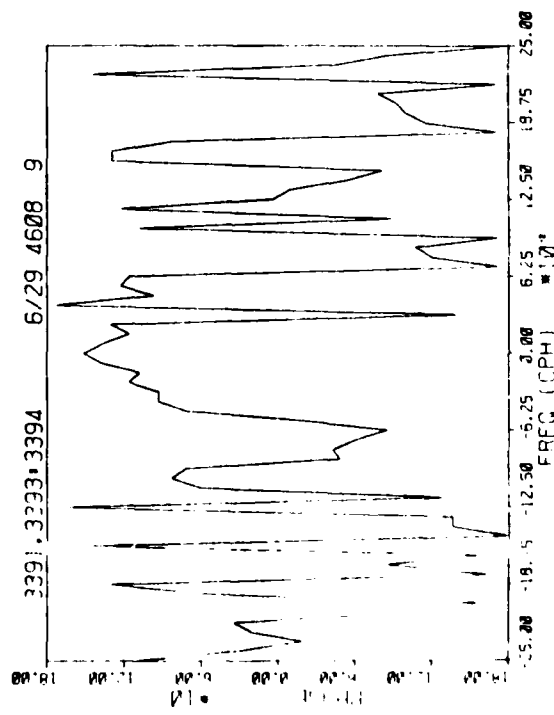
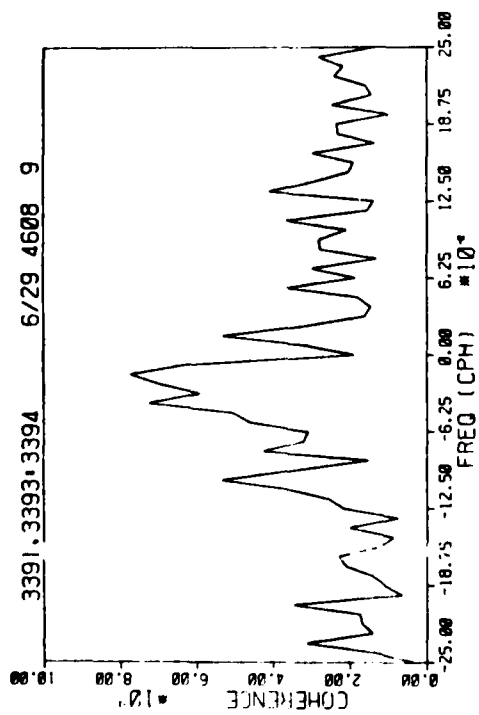
computed using the relation derived empirically by Amorocho and DeVries (1980):

$$C = 0.0015 \left[1 + \exp\left(\frac{|U| - 12.5}{1.56}\right) \right]^{-1} + 0.00104$$

4.4 COHERENCE ANALYSIS

We center our discussion of coherence on the coherence spectra of wind stress and vertical shear displayed in Figures 4.6 - 4.12. The shallowest shear records (12 - 32m) are coherent with the wind stress in the frequency band $0 > \omega > -f$ (see Figures 4.6 and 4.7). In the vicinity of the inertial frequency, the phase shifts by approximately 180° . This phase shift is expected because the surface layer is resonant at the inertial frequency. In the next pair of coherence spectra (Figures 4.8 and 4.9) between wind stress and shear at 32 - 52m, the coherence amplitude is not significant at the inertial ($f = -0.053$ cph). Figure 4.8 shows no significant coherence at the lowest frequencies $|\omega| < f$. Figure 4.9 shows a slight degree of coherence in the frequency band $|\omega| < f/2$. Of the three coherence spectra at the deepest levels (Figures 4.10 - 4.12; 52 - 72m), none show coherence peaks at the inertial frequency.

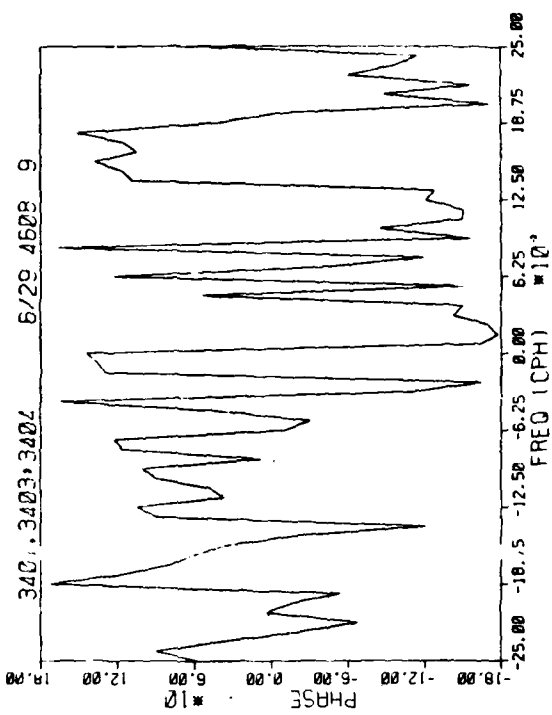
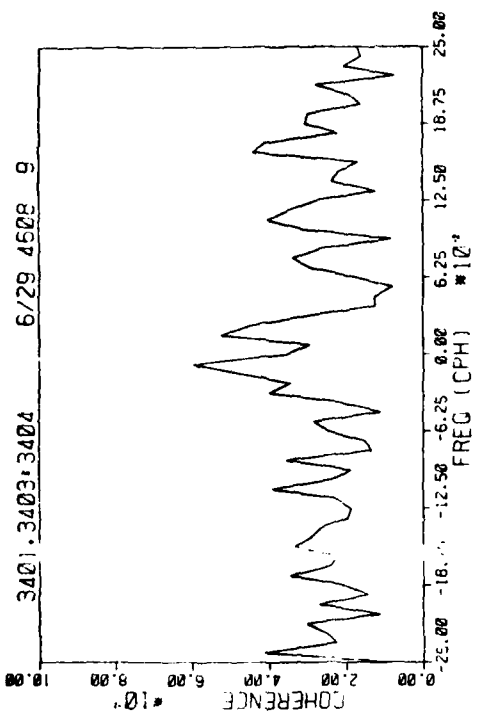
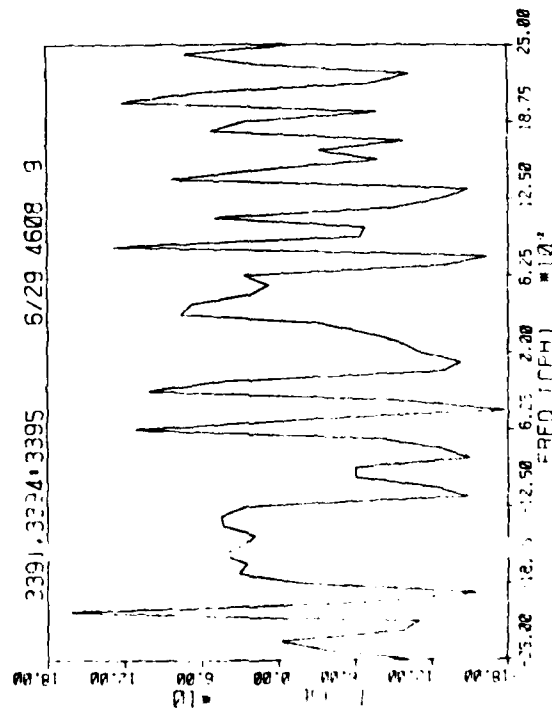
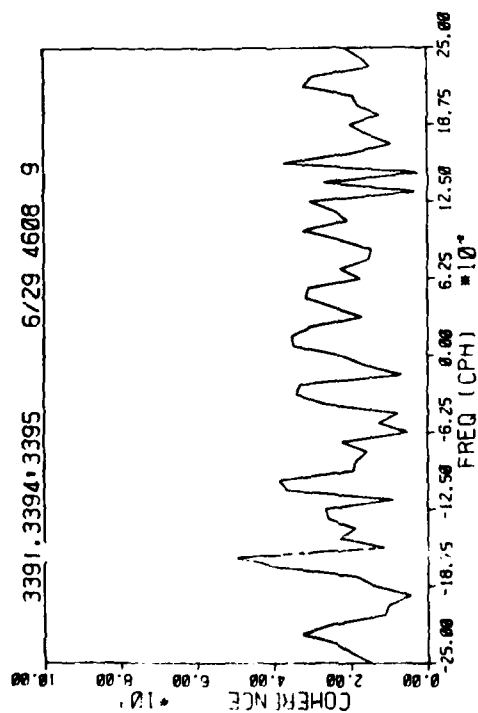
The coherence features discussed thus far are very similar to those found by Weller (1981). Weller observed the upper-ocean current by lowering vector measuring current meters from FLIP. Whereas in our data regime the mixed layer depth varied from 10 to 20m (see Figure 1.4), Weller's observations were taken in a regime where the mixed layer depth was about 50 m. Figure 4.13 shows coherence between



Wind Stress/Vertical Shear Coherence Amplitudes (Top) and Phases (Bottom).

Figure 4.6 (Left): Between 3391 and 3393-3394.

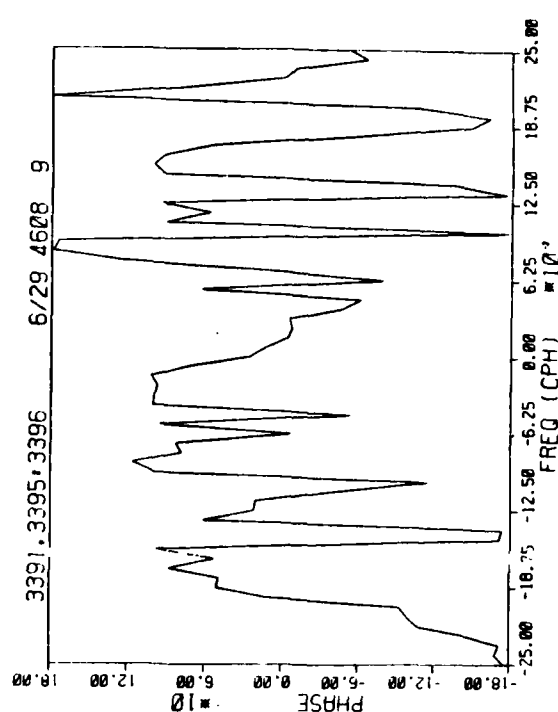
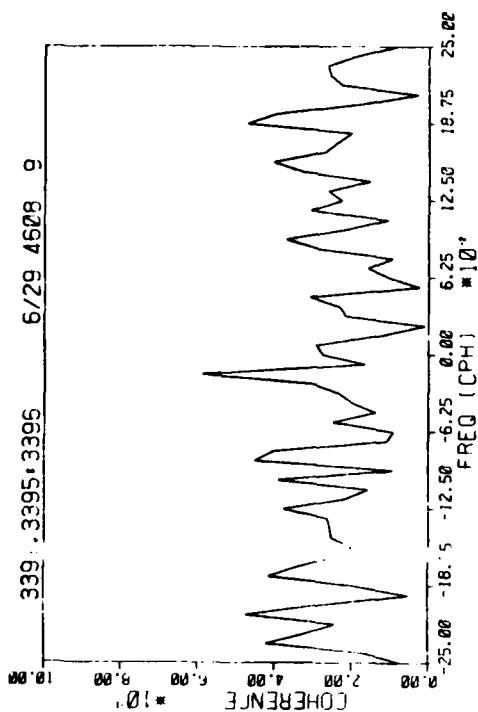
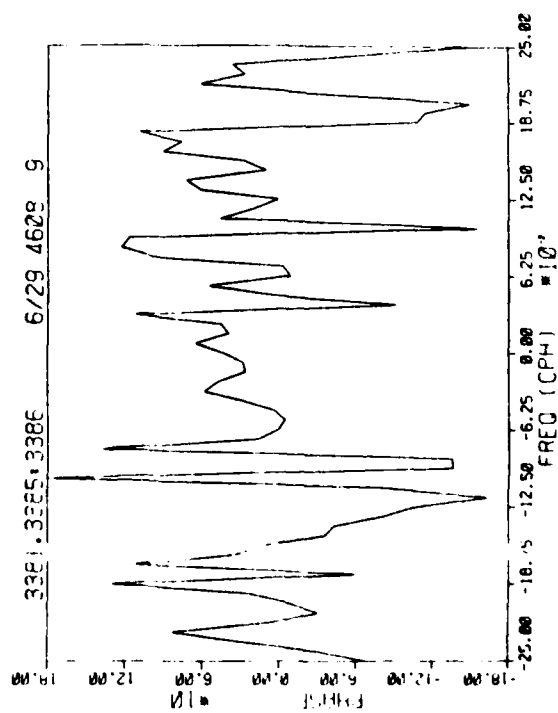
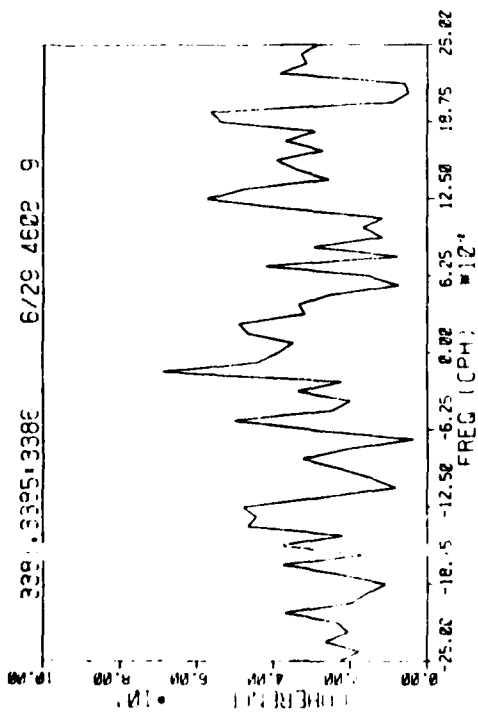
Figure 4.7 (Right): Between 3401 and 3402-3403.



Wind Stress/Vertical Shear Coherence Amplitudes (Top) and Phases (Bottom).

Figure 4.8 (Left): Between 3391 and 3394-3395.

Figure 4.9 (Right): Between 3401 and 3403-3404.



Wind Stress/Vertical Shear Coherence Amplitudes (Top) and Phases (Bottom).

Figure 4.10 (Left): Between 3381 and 3385-3386.

Figure 4.11 (Right): Between 3391 and 3395-3396.

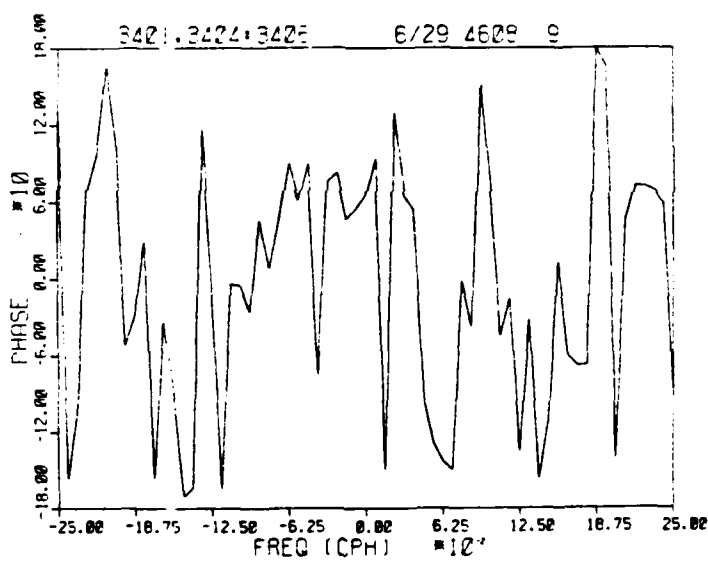
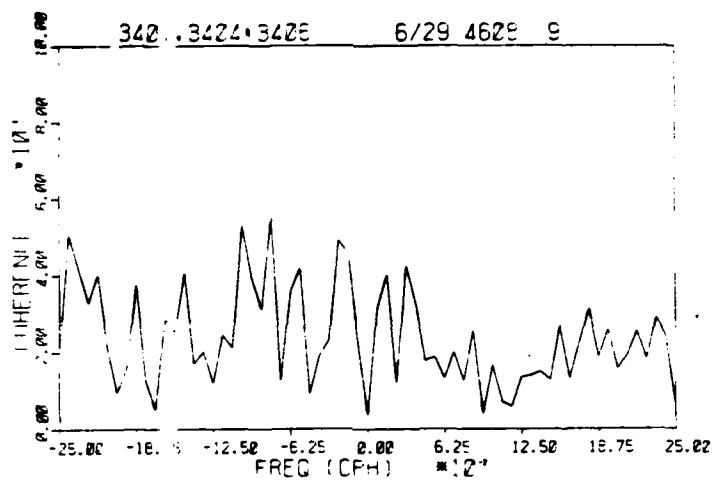


Figure 4.12 Wind Stress/Vertical Shear Coherence Amplitudes (Top) and Phases (Bottom). Between 3401 and 3404-3406.

wind stress and shear, as a function of depth and frequency. In this figure, the shear in the mixed layer is highly coherent in the frequency band $0 \gtrsim \omega \gtrsim -f$. The coherence extends deepest at the lowest frequencies, and at the inertial frequency. At the inertial frequency, there is no significant coherence between 50 and 80 m, but below 80 m, there is again significant coherence. Weller suggests downward propagating near-inertial waves, caused by local wind-induced Ekman suction as a possible explanation for this feature. It may also be possible that fluid in the region of the sharp density interface just below the surface layer is vertically advected past the current meters. This could result in shear records with discontinuities which tend to reduce the coherence with wind stress. In Rubenstein (1981a,b) we further discuss this mechanism, and give quantitative descriptions of internal wave propagation.

In addition to high coherence in the range $-f < \omega < 0$, two other interesting features show up in Figures 4.6 and 4.7. In Figure 4.9 there is a coherence peak which just reaches the significance level at $\omega = 2f = -.105$ cph. In Figure 4.7 there is a strong coherence peak at $\omega = f + \omega_s = -.138$ cph (where ω_s denotes the semidiurnal frequency). We discussed in Section 3 the evidence for nonlinear interactions between inertial oscillations and semidiurnal tides. These nonlinear interactions showed up in the shear power spectra as small peaks at $\omega = f + \omega_s$ (see Section 3.3.4). We are probably seeing the coherence between some combination of the following nonlinear effects:

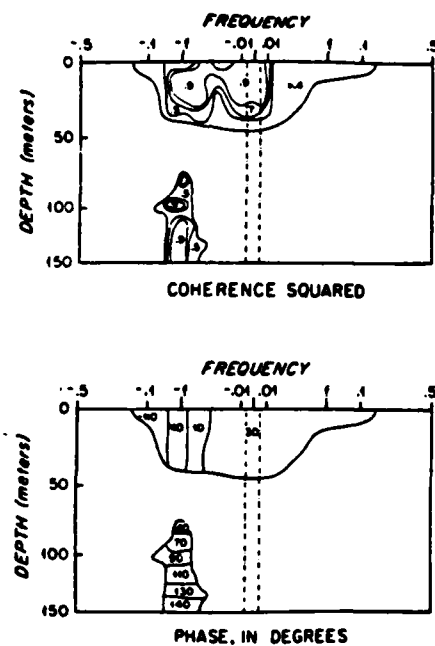


Figure 4.13 Coherence (top) and phase (bottom) between the wind stress and the shear. Positive angles indicate shear is to the right of the wind stress. From Weller (1981).

1. There are usually strong shears associated with the sharp density interface at the base of the mixed layer. These shears are not likely to be linear in depth. A pair of current meters located in the vicinity responds nonlinearly to small vertical displacements of the interface.
2. We use an imperfect parameterization in calculating the wind stress. The deviation of this parameterization from the true wind stress is a nonlinear function of the wind speed.
3. The motion of the surface buoy responds in a nonlinear way to changes in the direction of the wind and surface current. Information about the motion of the buoy may be transmitted through the mooring line to the individual current meters. These effects may be complicated even further by motions caused by the drag of the mooring line itself.
4. Assume that the power at the sum frequency $f + \omega_s$ is partially due to the nonlinear interaction between semi-diurnal tidal oscillation and a local wind-induced inertial oscillation. Then shear at the sum frequency is indirectly correlated with the wind at the inertial frequency. Assume, in addition, that the spectral shape of wind stress is stationary. Power levels at all frequencies then rise and fall in unison. Thus there will be coherence between wind stress and shear at the sum frequency, but this coherence does not imply a direct causal relationship.

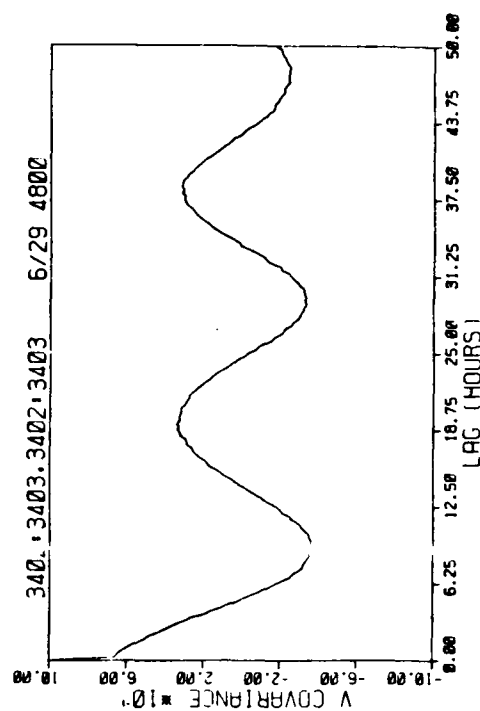
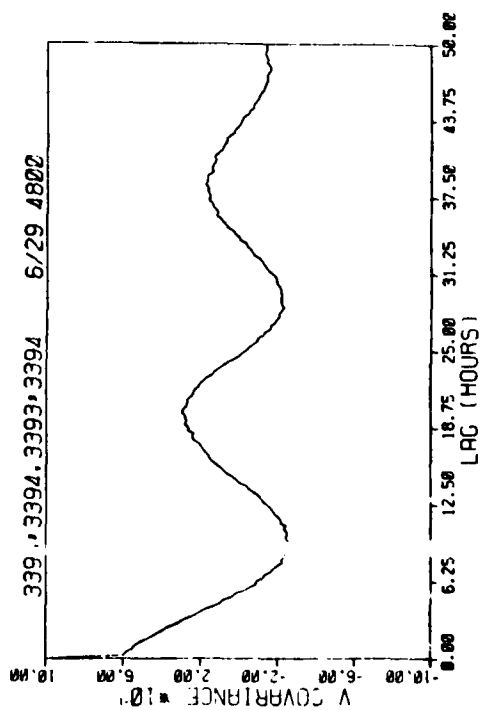
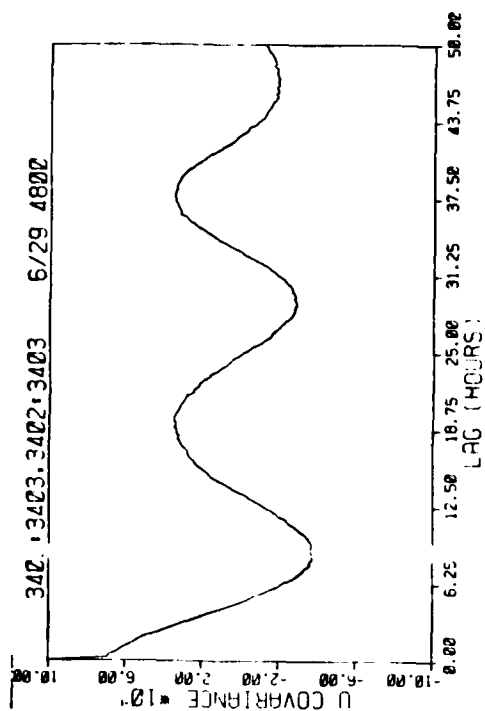
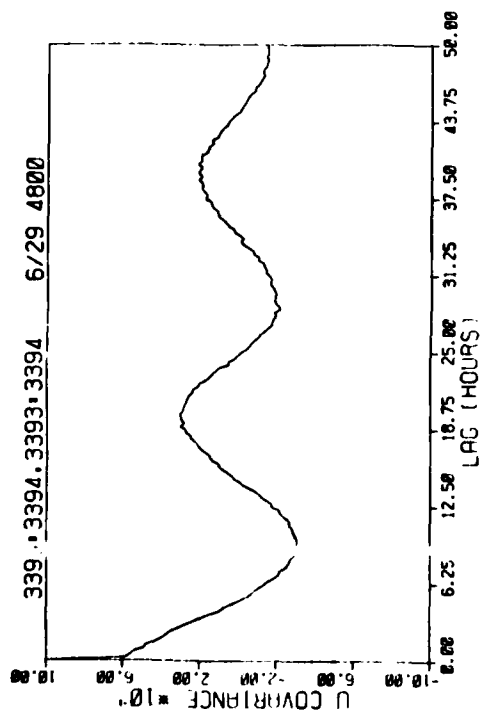
Section 5

CORRELATION FUNCTIONS

Auto-correlation functions, as well as vertical, horizontal, and slant separation cross-correlation functions were computed for vertical shear measurements. Separate calculations were performed for the x- and y-direction components of the shear. The measurements were not filtered prior to computing the correlation functions. As a result, spikes appear at zero lag for the auto-correlations and the vertical separation cross-correlations. It was found that smoothing the data records with a three-point triangle weighting function was sufficient to remove the spikes. But this smoothing was not performed for the figures displayed in the present report. Future reports may examine the appropriateness of such filtering.

5.1 AUTO-CORRELATIONS OF VERTICAL SHEAR

Because the auto-correlation functions of vertical shear are all much alike, only two example auto-correlation functions are displayed in Figures 5.1 and 5.2. Since auto-correlation functions are symmetric, only the positive sides are plotted. The spikes at zero lag are discussed above. The strong ringing has a crest-to-crest duration equal to the inertial period, about 19 hours. The amplitude of the ringing decreases with increasing depth because inertial energy becomes a smaller percentage of the total energy as depth increases. This can also be seen in the frequency spectra shown in Figures 3.3 - 3.9. Such strongly periodic auto-correlation functions near the surface suggest that when



Auto-Correlation Functions of Vertical Shear, U-Components (Top) and V-Components (Bottom).

Figure 5.1 (Left): 3393-3394.

Figure 5.2 (Right): 3402-3403.

inertial motions are the dominant motion, the shear field becomes rather deterministic. Thus a single velocity profile measurement together with the knowledge of dominant inertial motions might allow the reconstruction at an earlier point in time of the shape of an hydrodynamic feature in order to obtain clues as to it's possible origin.

5.2 CROSS-CORRELATIONS OF HORIZONTALLY, SLANT, AND VERTICALLY SEPARATED VERTICAL SHEAR

The cross-correlations of horizontally, slant, and vertically separated vertical shear measurements are listed in Tables 5.1, 5.2, and 5.3, respectively, and are displayed in Figures 5.3 - 5.21. Since cross correlation functions are not symmetric, both sides (positive and negative) sides are displayed. Positive lags indicate that the second pair of vertically differenced current measurements was being lagged with respect to the first pair. As in the auto-correlation functions, the ringing behavior appears to be ubiquitous, with a crest-to-crest duration equal to the inertial period.

5.3 CROSS-CORRELATION ANALYSIS

The cross-correlation between two sinusoidal time series is also a sinusoidal function. If the two time series are shifted in phase with respect to one another, then this phase shift may readily be ascertained from the cross-correlation function. In this section we present estimates of the phase shifts shown by the horizontally, vertically, and slant separated cross-correlation functions.

Table 5.1
CROSS-CORRELATIONS OF HORIZONTALLY SEPARATED
VERTICAL SHEAR MEASUREMENTS

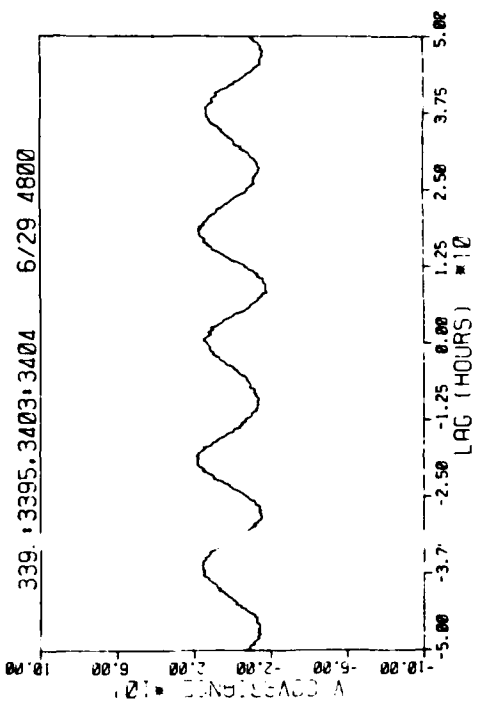
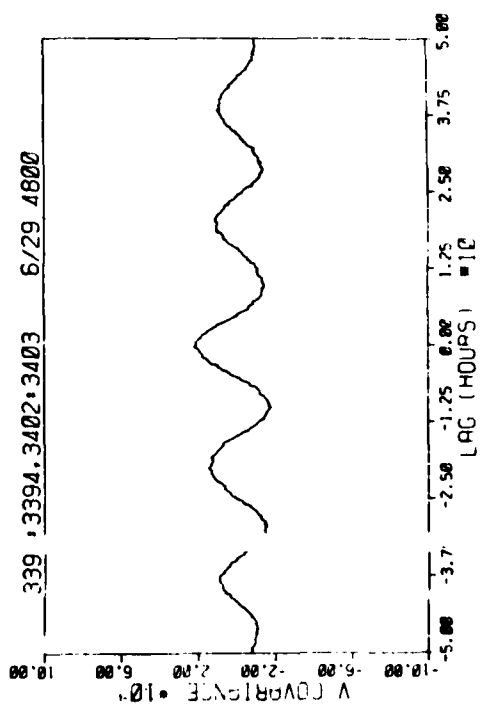
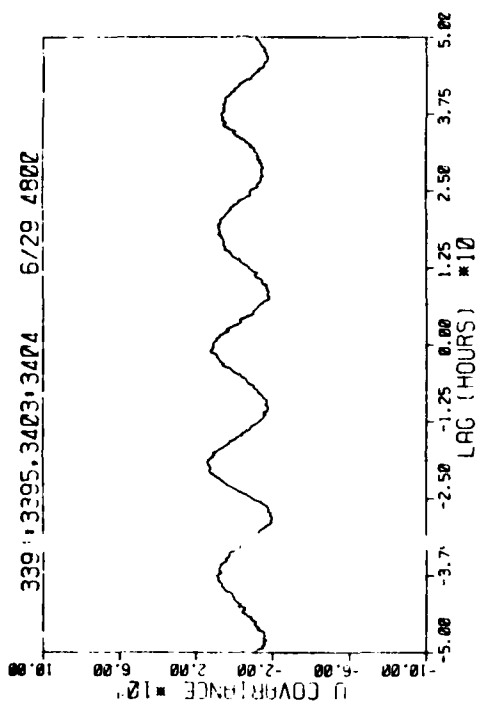
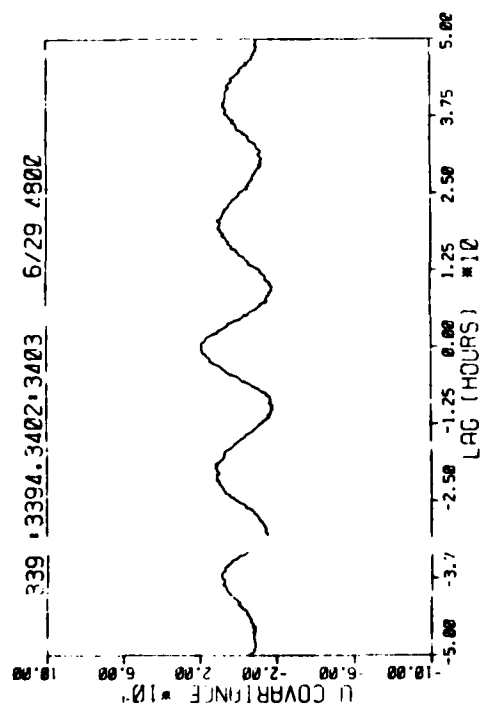
<u>Fig.</u>	<u>Current Meters</u>	<u>Depths (m)</u>
5.3	3393-3394/3402-3403	12-32
5.4	3394-3395/3403-3404	32-52
5.5	3395-3396/3404-3406	52-72
5.6	3395-3396/3385-3386	52-72
5.7	3404-3406/3385-3386	52-72

Table 5.2
CROSS-CORRELATIONS OF SLANT SEPARATED VERTICAL
SHEAR MEASUREMENTS

<u>Fig.</u>	<u>Current Meters</u>	<u>Depths (m)</u>
5.8	3393-3394/3403-3404	12-32/32-52
5.9	3393-3394/3404-3406	12-32/52-72
5.10	3394-3395/3402-3403	32-52/12-32
5.11	3394-3395/3404-3406	32-52/52-72
5.12	3395-3396/3402-3403	52-72/12-32
5.13	3395-3396/3403-3404	52-72/32-52
5.14	3385-3386/3393-3394	52-72/12-32
5.15	3385-3386/3394-3395	52-72/32-52
5.16	3385-3386/3402-3403	52-72/12-32
5.17	3385-3386/3403-3404	52-72/32-52

Table 5.3
CROSS-CORRELATIONS OF VERTICALLY SEPARATED
VERTICAL SHEAR MEASUREMENTS

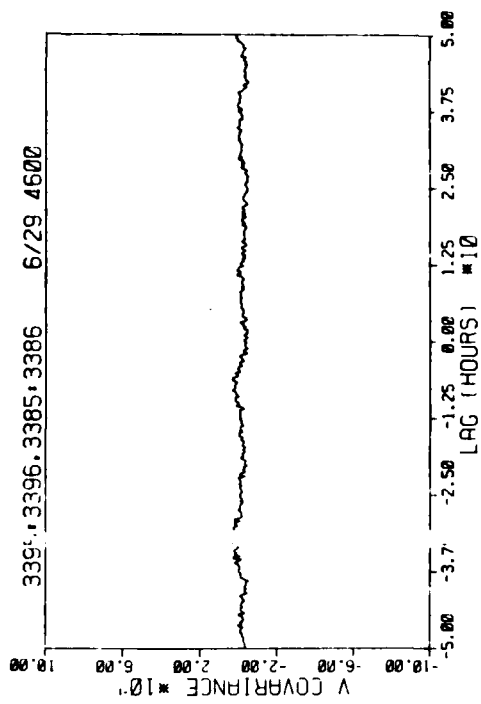
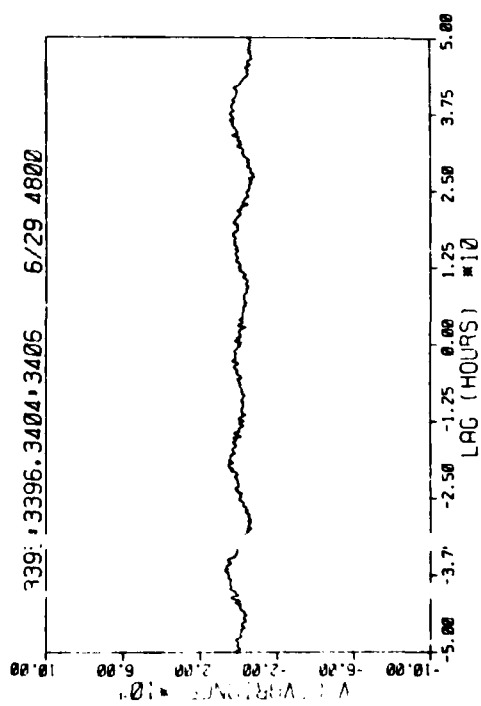
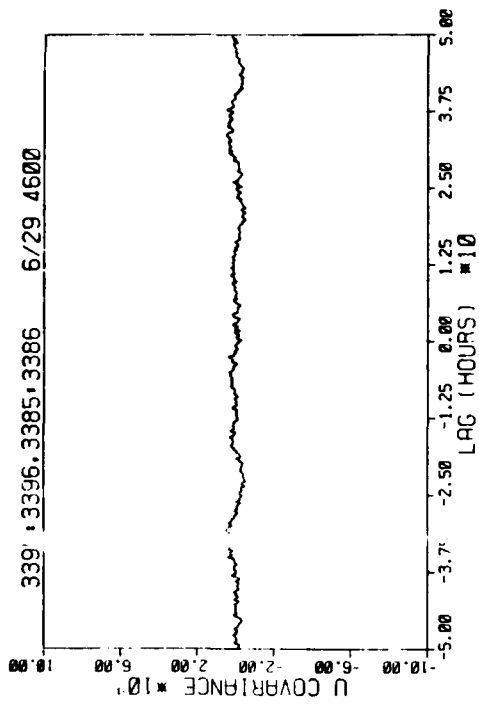
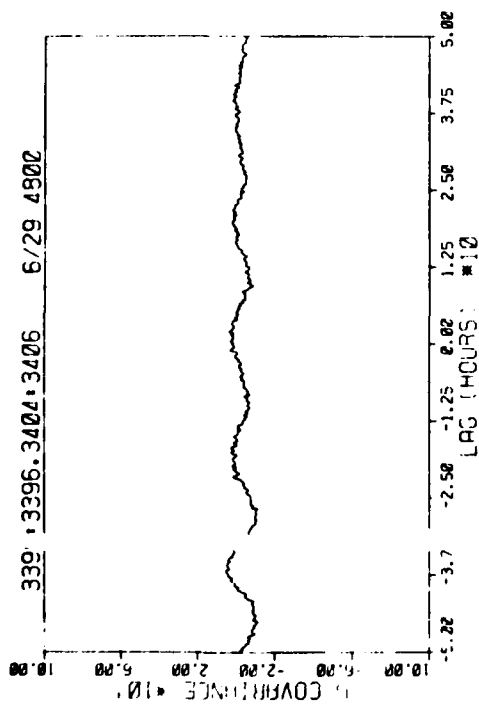
<u>Fig.</u>	<u>Current Meters</u>	<u>Depths (m)</u>
5.18	3393-3394/3394-3395	12-32/32-52
5.19	3402-3403/3403-3404	12-32/32-52
5.20	3394-3395/3395-3396	32-52/52-72
5.21	3403-3404/3404-3406	32-52/52-72



Cross-Correlation Functions of Horizontally Separated Vertical Shear,
U-Components (Top) and V-Components (Bottom).

Figure 5.3 (Left) Between 3393-3394 and 3402-3403.

Figure 5.4 (Right): Between 3394-3395 and 3403-3404.



Cross-Correlation Functions of Horizontally Separated Vertical Shear,
U-Components (Top) and V-Components (Bottom).

Figure 5.5 (Left): Between 3395-3396 and 3404-3406.

Figure 5.6 (Right): Between 3395-3396 and 3385-3386.

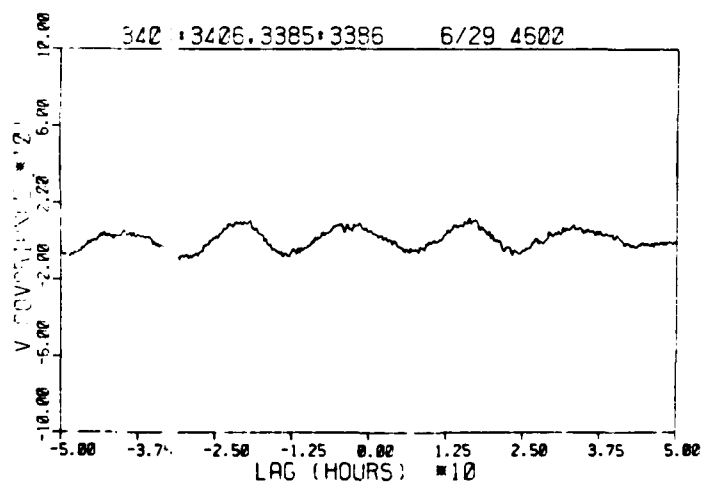
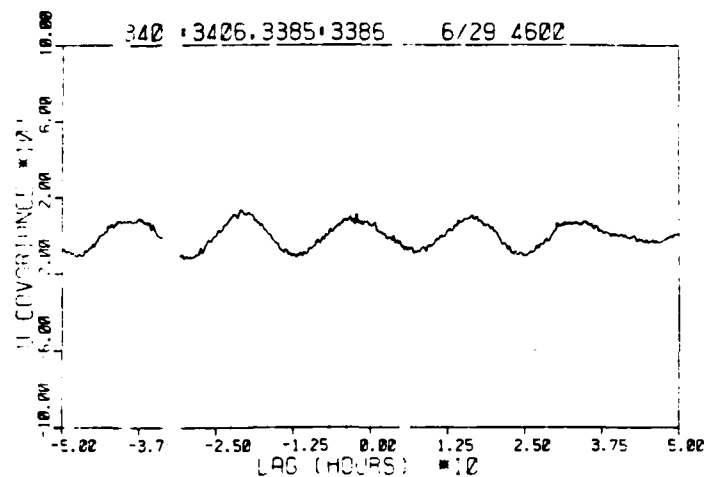
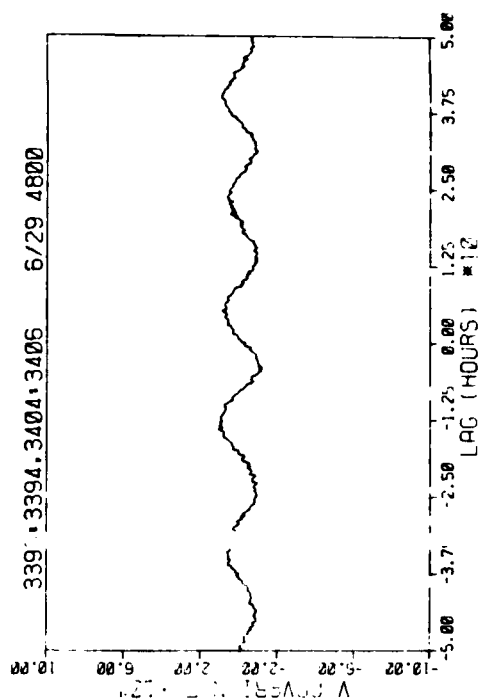
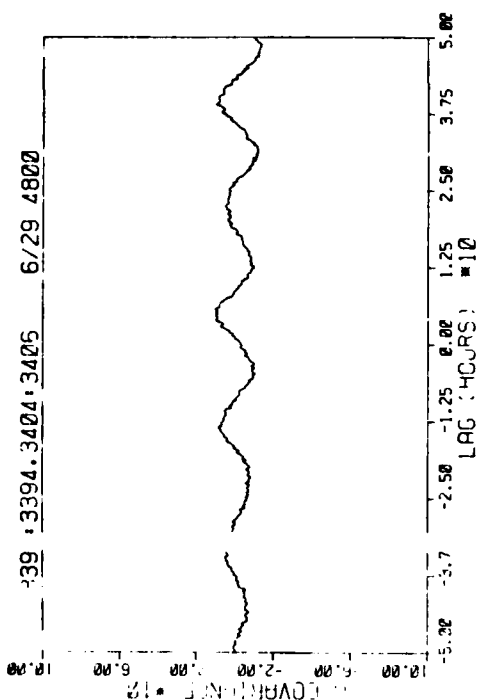


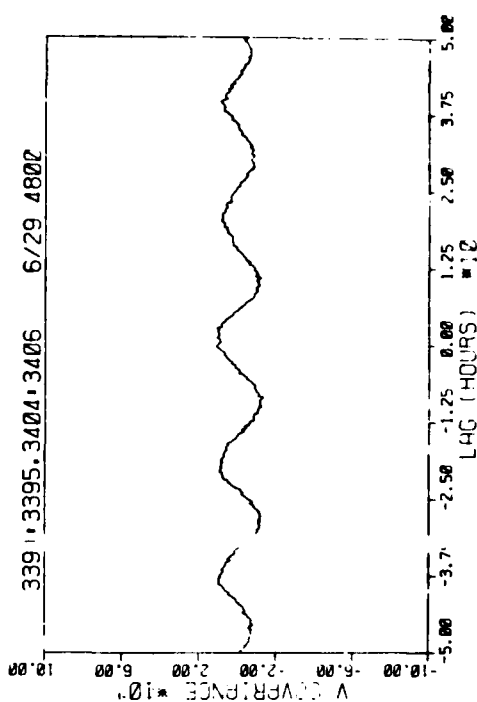
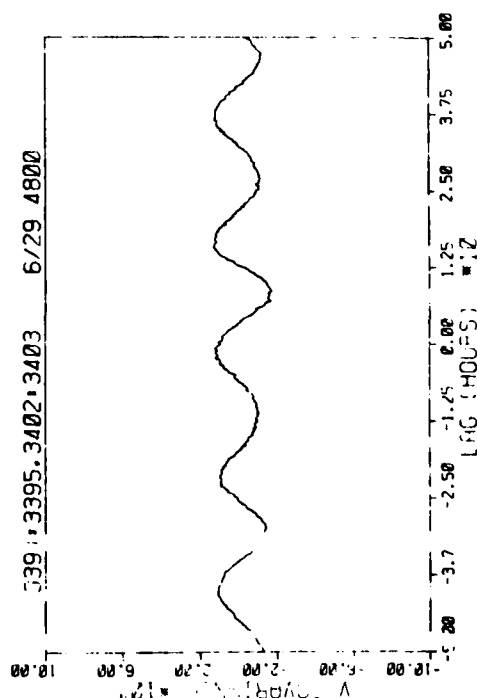
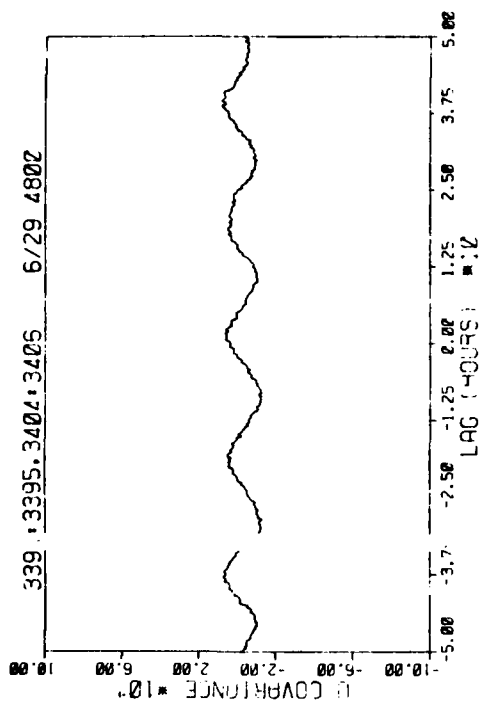
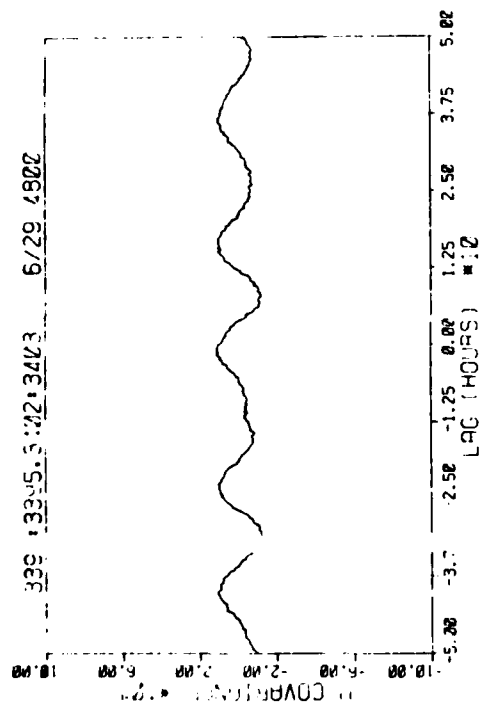
Figure 5.7 Cross-Correlation Functions of Horizontally Separated Vertical Shear, U-Component (Top) and V-Component (Bottom), Between Current Meters 3404-3406 and 3385-3386.



Cross-Correlation Functions of Slant Separated Vertical Shear,
U-Components (Top) and
V-Components (Bottom).

Figure 5.8 (Left): Between 3393-3394 and 3403-3404.

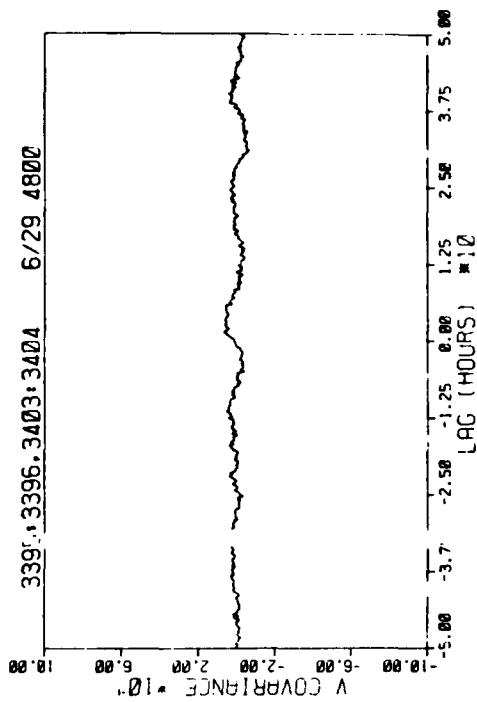
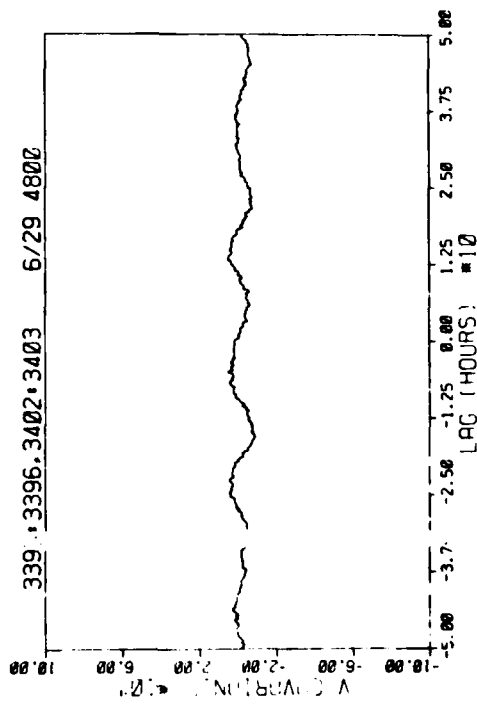
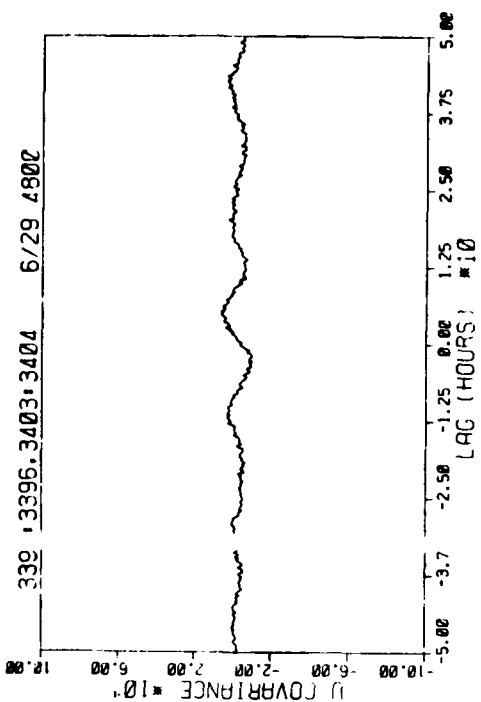
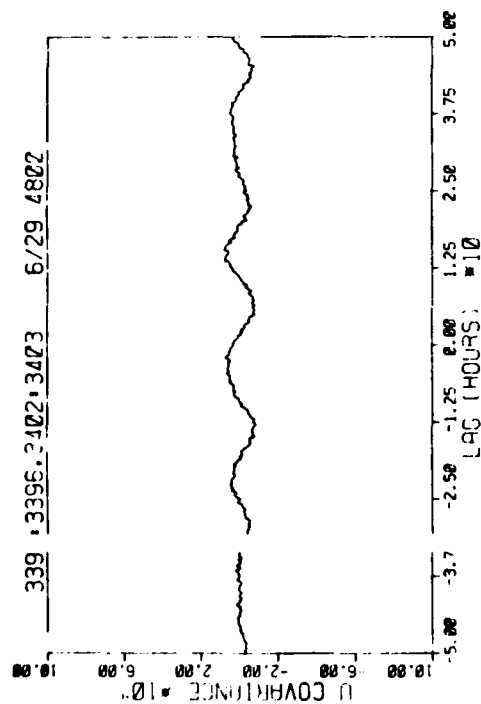
Figure 5.9 (Right): Between 3393-3394 and 3404-3406.



Cross-Correlation Functions of Slant Separated Vertical Shear,
U-Components (Top) and V-Components (Bottom).

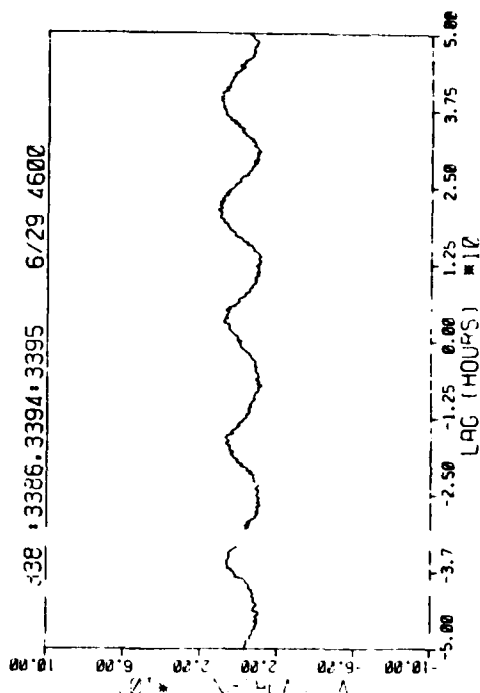
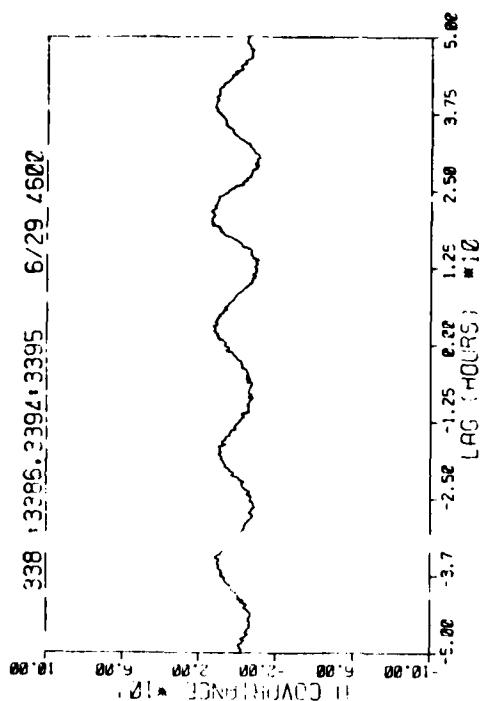
Figure 5.10 (Left): Between 3394-3395 and
3402-3403.

Figure 5.11 (Right): Between 3394-3395 and
3404-3406.



Cross-Correlation Functions of Slant Separated Vertical Shear,
U-Components (Top) and
V-Components (Bottom).

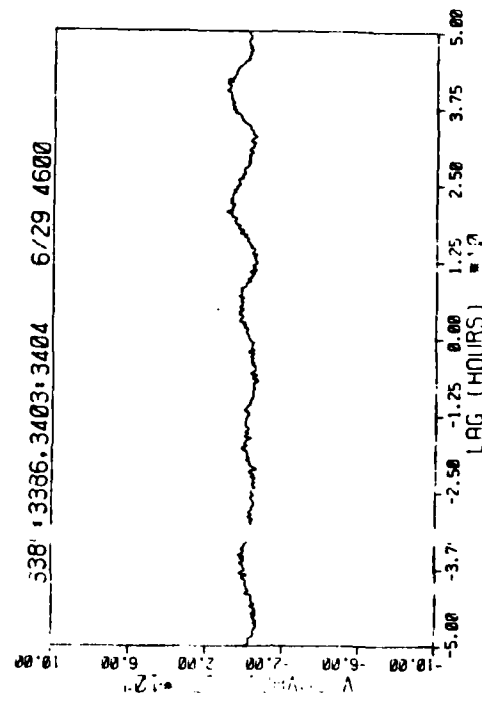
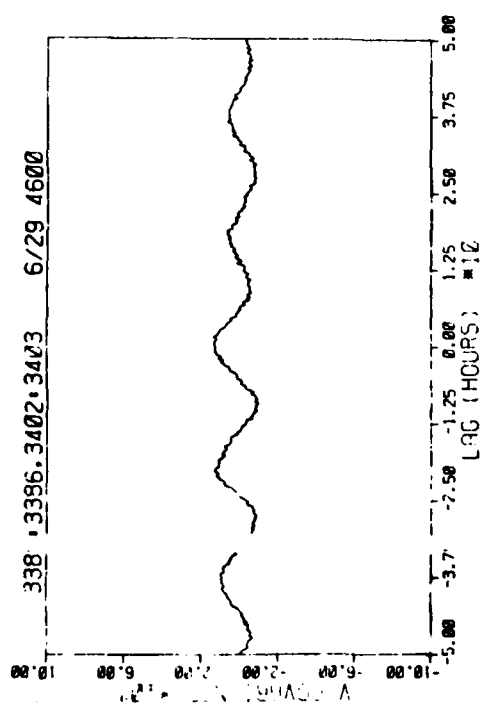
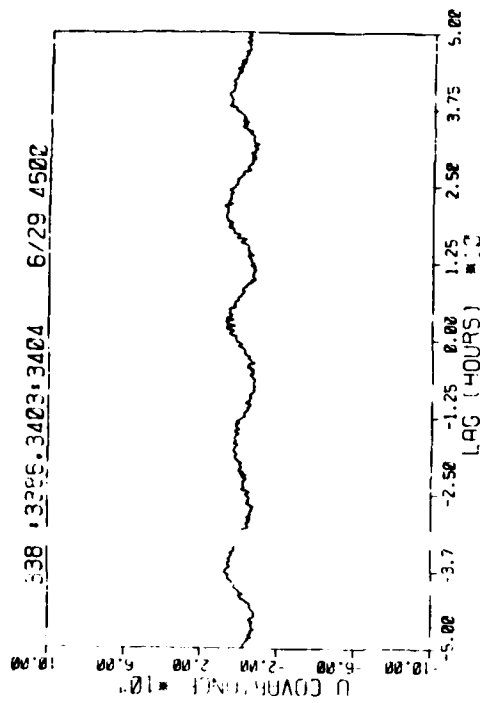
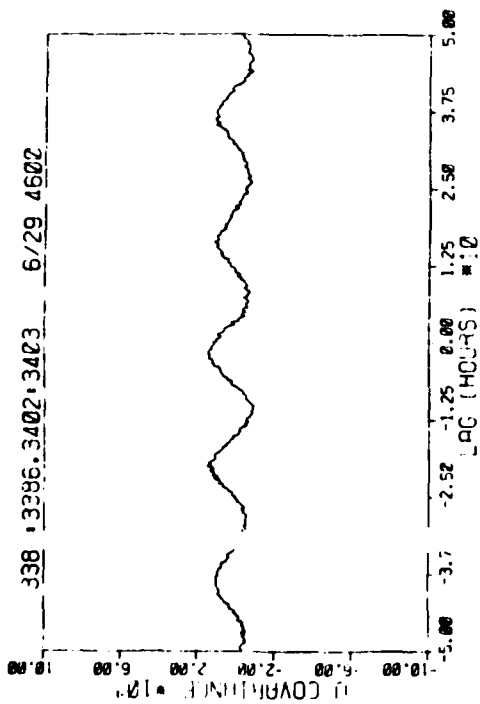
Figure 5.12 (Left): Between 3395-3396 and 3402-3403.
Figure 5.13 (Right): Between 3395-3396 and 3403-3404.



Cross-Correlation Functions of Slant Separated Vertical Shear,
U-Components (Top) and
V-Components (Bottom).

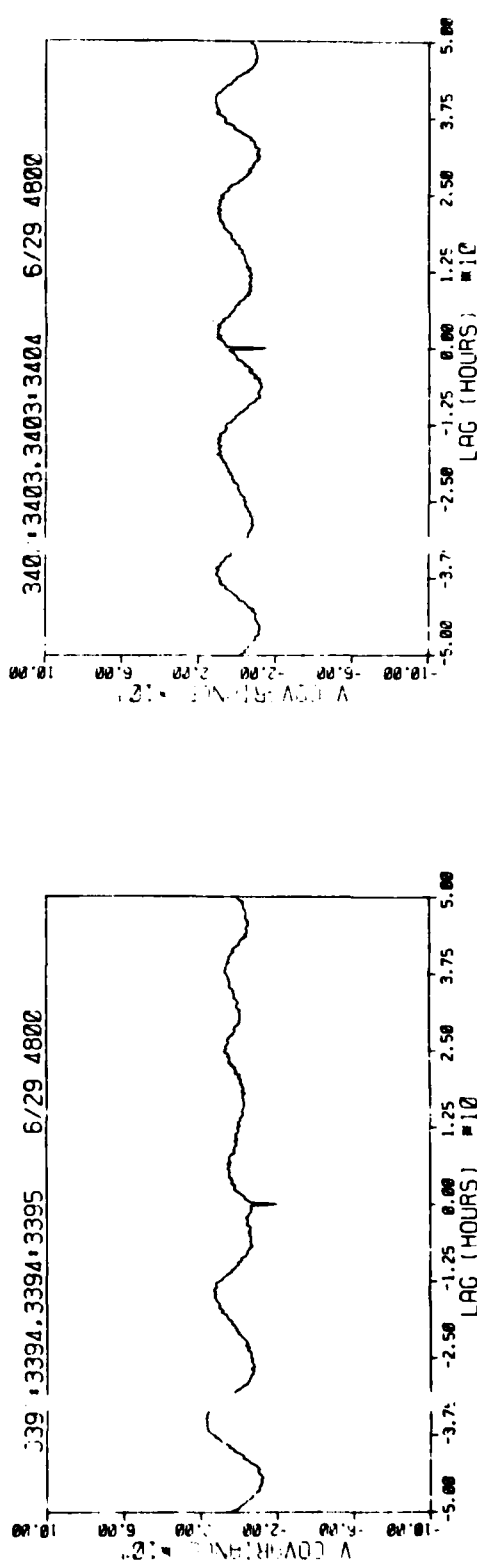
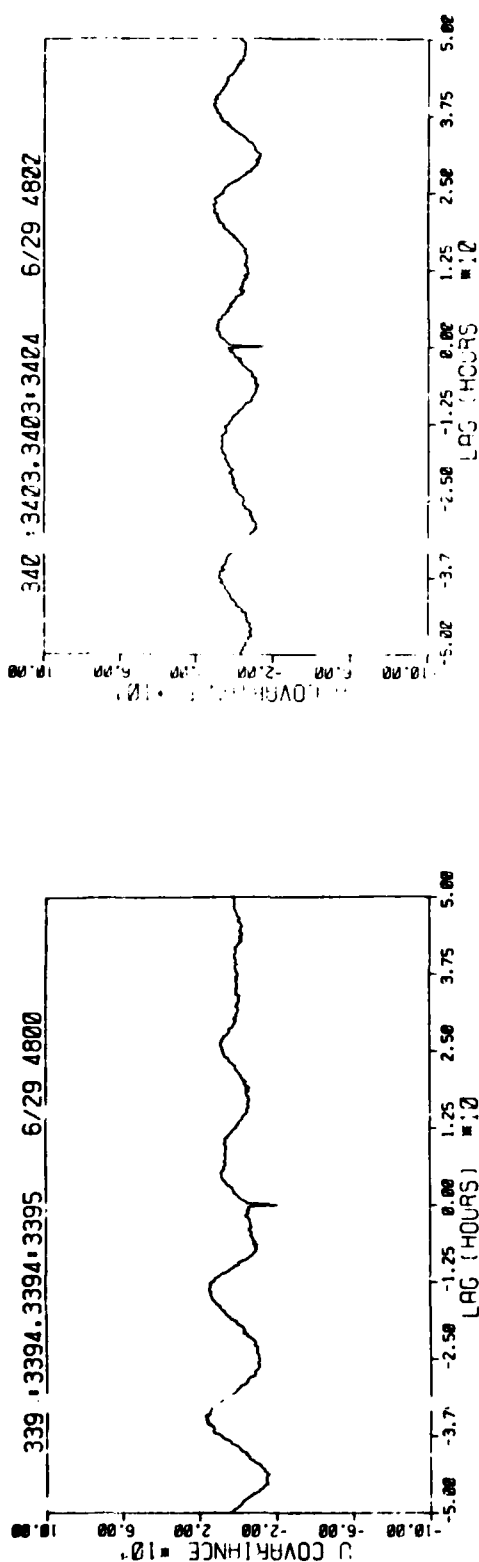
Figure 5.14 (Left): Between 3385-3386 and 3393-3394.

Figure 5.15 (Right): Between 3385-3386 and 3394-3395.



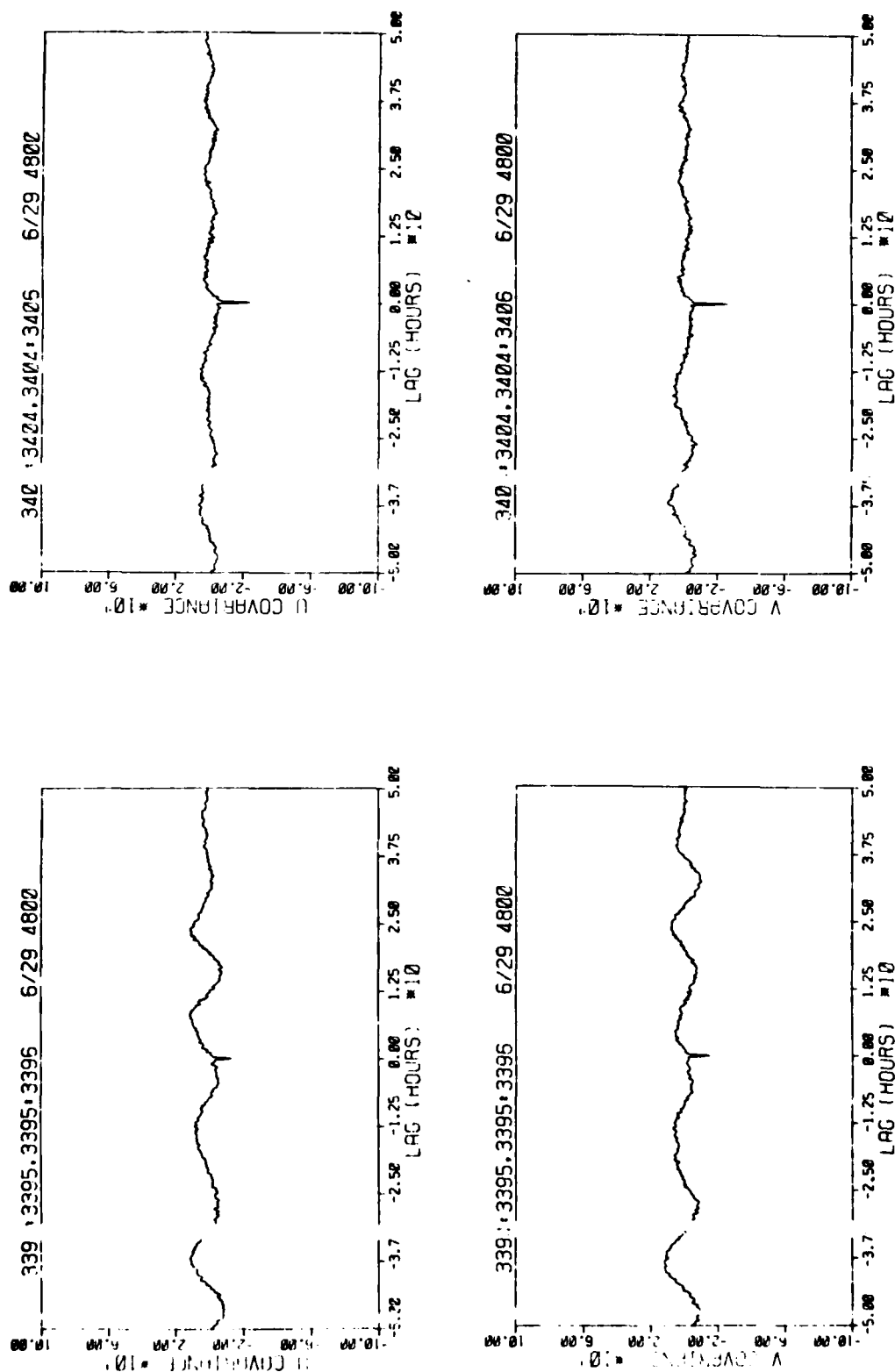
Cross-Correlation Functions of Slant Separated Vertical Shear,
U-Components (Top) and
V-Components (Bottom).

Figure 5.16 (Left): Between 3385-3386 and 3402-3403.
Figure 5.17 (Right): Between 3385-3386 and 3403-3404.



Cross-Correlation Functions of Vertically Separated Vertical Shear,
U-Components (Top) and
V-Components (Bottom).

Figure 5.18 (Left): Between 3393-3394 and 3394-3395.
Figure 5.19 (Right): Between 3402-3403 and 3403-3404.



Cross-Correlation Functions of Vertically Separated Vertical Shear,
 U-Components (Top) and
 V-Components (Bottom).

Figure 5.20 (Left): Between 3394-3395 and 3395-3396.
 Figure 5.21 (Right): Between 3403-3404 and 3404-3406.

Figure 5.22 schematically shows the current meters, and the cross-correlation phase shifts between them. Only the deepest two current meters from mooring 338 are shown, as there is no data from the 32 m current recorder 3384 so there is no shear time series for the pair 3383-3384. The lines join those pairs of current meters for which the cross-correlation functions of velocity differences show significant periodicity with an inertial period. Beside each line is the estimated phase shift, in degrees. We estimate the resolution limit for our phase shift estimates to be about 20° . The arrow through each line points toward the lagging pair of current meters. The circled arrows denote significant asymmetry in the cross-correlation functions.

With but one exception (3394-3395 to 3385-3386), the arrows for the slant and vertical cross-correlations all point from the lower toward the upper pair of current meters. This result implies that the phase velocity of these near-inertial oscillations is directed upward. From the estimated phase shift we can estimate the values of phase velocity and vertical wavelength. The phase shifts associated with the vertical cross-correlations range from 60° to 110° , corresponding to upward phase velocities of $1-2 \times 10^{-3}$ m/sec. This range corresponds to vertical wavelengths between 67 and 134 m.

The two uppermost horizontal cross-correlations both show zero phase lag. Therefore we can only put a lower limit on the horizontal wavelength in the direction between moorings 339 and 340. Our estimated resolution limit of $\pm 20^\circ$ implies that the predominant horizontal wavelength is at least 1000 km. We remind the reader that these cross-correlation functions were obtained over a 50 day period, and

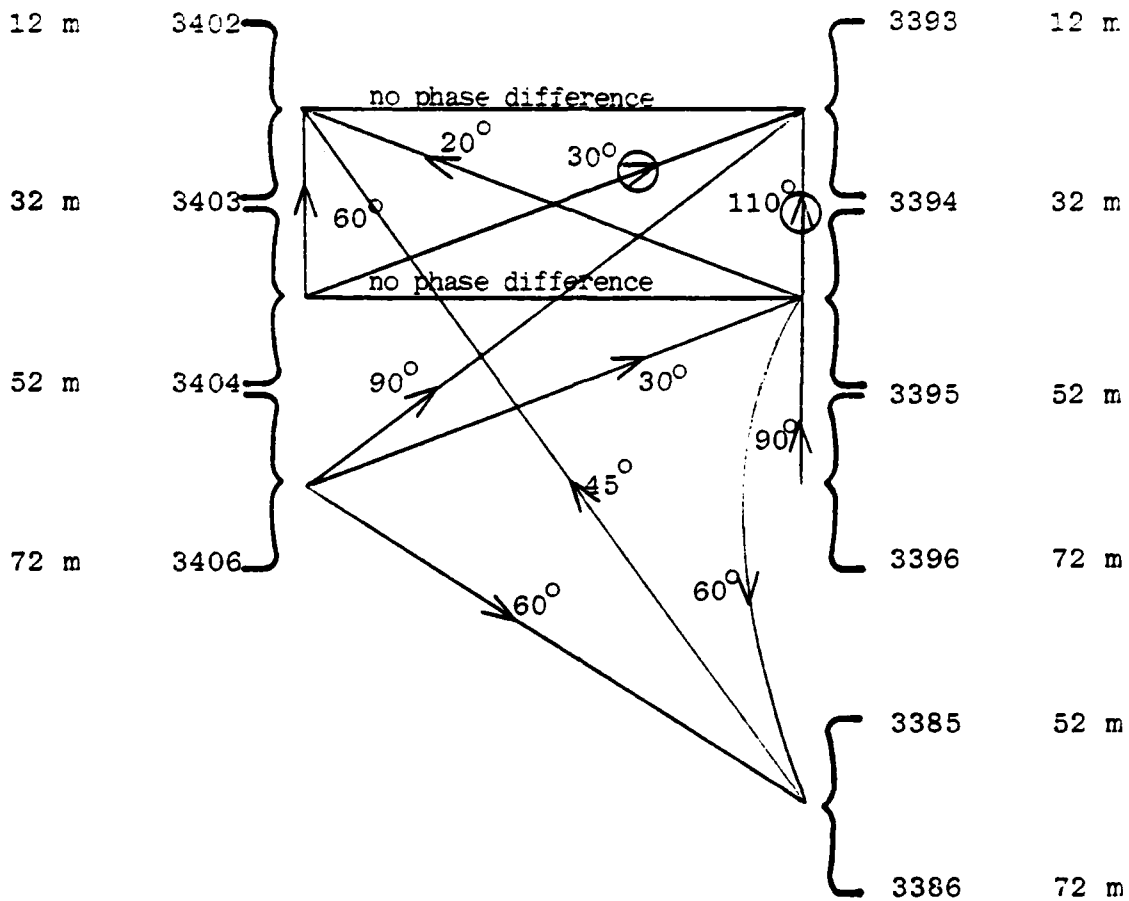


Figure 5.22: Cross-Correlation Phase Shifts Between Current Meter Pairs. Lines join current meter pairs whose velocity-difference cross-correlations exhibit significant periodicity with an inertial period. Numbers are phase shifts in degrees, and arrows point toward the lagging pair of current meters (i.e., in the direction of phase propagation). Circled arrows denote asymmetry in the cross-correlations.

that during portions of this period the predominant horizontal wavelength may be quite different.

Two of the arrows in Figure 5.22 are circled, indicating marked asymmetry in the correlation functions with respect to zero lag. This asymmetry shows stronger inertial periodicity for negative lags than for positive lags. This implies that the upper pair of current meters undergoes near-inertial oscillations before the lower pair. This result agrees with our understanding that the oscillations are wind-induced, and that the direction of energy propagation (the direction of the group velocity) is directed downward.

Section 6
SUMMARY AND CONCLUSIONS

We have analyzed vertical shear time series obtained from 48-day current meter records obtained by R. Pollard in 1970. Three moorings in a triangular array were spaced 50 and 70 kilometers apart. Each contained current meters at 12, 32, 52 and 72 meters depth. One instrument at 32 meters depth failed to give any data. The moorings were located on the continental slope south of New England at depths of 2400 to 2600 meters. Two atmospheric frontal systems passed over the moorings near the beginning and end of the time series. These fronts caused energetic inertial oscillations which dominate the upper current meter records for several days following the disturbances.

Vertical shear was computed by simply taking the difference between velocities recorded by vertically adjacent current meters and dividing by the 20 meter sensor spacing. Because of the large vertical sensor spacing, frequency spectra of vertical shear contain only a portion of the total shear variance. Based on a spectral model of shear described by Grabowski and Newman (1981), we estimate that sensors 20 meters apart in depth will detect 54% of the shear variance which would be measured by sensors 10 meters apart and 14% of the shear variance which would be measured by sensors spaced 2 meters apart. Sensor spacing probably has little effect, however, on the observed shape of the frequency spectrum below 2 cph, the highest frequency considered in this analysis. Therefore, only spectral power density levels are affected.

Frequency spectra of all the shear time series contain strong peaks in the neighborhood of the inertial frequency (0.053 cph or 9.3×10^{-5} rad/sec). The variance associated with the inertial peaks decreases with increasing depth. Vertical shear at inertial frequencies is created largely by the rapid decay of velocity amplitude with distance from the surface. That is, inertial velocities recorded at the upper end of a given 20 meter interval are substantially greater than those recorded at the lower end.

Frequency spectra of shear also show a distinct peak at the semidiurnal frequency, but such peaks typically contain substantially less energy than an inertial peak in the same spectrum. The peak near the semidiurnal frequency is present because the semidiurnal tide is strongly baroclinic in the New England slope region. According to Regal and Wunsch (1973), the baroclinic semidiurnal tide is due to the interaction of the barotropic tide with the continental slope. However, the semidiurnal tide is not expected to contribute significantly to frequency spectra of near surface shear in the open ocean.

Shear spectral density levels were found to increase with frequency in a band from 0.5 to 2.0 cph. This effect may be due to aliasing of the internal wave motions at frequencies higher than 2.0 cph. An example of the aliasing effect was discussed based on the Garrett and Munk internal wave spectrum. Mooring motion may be another factor contributing to the spectral level increase with frequency.

Evidence of a possible nonlinear interaction between motions at inertial and semidiurnal frequencies was found in a spectral peak at a frequency equal to the sum of the inertial and semidiurnal frequencies. Wave motions at this sum frequency can propagate into the stratified interior and thereby provide radiative damping of inertial motions. Other suggested dissipation mechanisms are Kelvin-Helmholtz instability (Pollard et al., 1973) and radiating internal waves generated by differentially advected mixed layer turbulence inducing undulation of the seasonal thermocline (Bell, 1978).

Because of the failure of one 32m current meter, horizontal coherence was computed for only one pair of shear time series in the 12-32 meter range. This horizontal coherence spectrum (over a distance of 50 kilometers) showed significant coherence in the frequency range, $-f < \omega < 0$. The corresponding phase spectrum fluctuates about zero in the same frequency range implying a horizontal wavelength very long compared to 50 kilometers.

Coherence of shear with wind stress was significant at approximately 0.7 in the band $-f < \omega < 0$, with an expected resonant phase shift of 180° near $\omega = -f$. In the depth intervals 32-52 meters and 52-72 meters, almost no significant coherence was found between shear and wind stress. The latter observation is consistent with the propagation of near-inertial oscillations into these depth intervals along very gently downward sloping characteristics from a remote surface location, forced by the wind stress at an earlier time. Some similarities were observed between these results and those of Weller (1981) derived from data taken by profiling current meters from FLIP.

Some peaks in coherence between wind stress and shear were also found at $\omega = -2f$ and $\omega = -(f+\omega_s)$ where ω_s is the semidiurnal frequency. They may be 1) artifacts of the measurement, due to use of discrete sensors; 2) effects of imperfect parameterization in calculating wind stress, or 3) effects due to correlation between changing power levels of a constant shape wind spectrum and the corresponding changes in level of inertial-tidal interaction.

Vertical, horizontal, and slant cross-correlation functions were computed for the vertical shear time series. All of the vertical cross correlation functions and all but one of the slant cross correlation functions show upward phase propagation corresponding to phase velocities in the range $1-2 \times 10^{-3}$ m/sec, and vertical wavelengths in the range 67-134 meters. Two of the cross-correlation functions have amplitudes that are larger for negative than for positive lags. The implication is that internal wave packets propagate downward, away from the near-surface region of generation.

Several conclusions may be drawn regarding the open ocean near surface shear observed in this data set. First, because the data were obtained in deep water well away from land, they should represent open ocean conditions rather well with the one exception of the shear caused by the strongly baroclinic semidiurnal tide. In the open ocean the semidiurnal tide is barotropic and cannot produce shear. Second, it is clear from these data that inertial motions can cause a large fraction of the shear calculated over a vertical scale of 20 meters. Consequently, the vertical shear field

exhibits some horizontal and vertical scales associated with inertial motions. Third, since dissipation times for inertial motions are of the order of several days, and typical intervals between passages of atmospheric fronts may be comparable in northern areas, then inertial motions may exist much of the time. This implies that the shear field may have a large inertial component and therefore in fact be quasi-periodic much of the time. Fourth, fifteen minute sample intervals are too long and cause aliasing of the internal wave induced shear. The shorter 112.5 second sample intervals used on Vector Averaging Current Meters (VACMs) are much more likely to sample all important internal wave frequencies adequately. Finally, although some effects of mooring motion may be subtracted out when differencing velocity time series, coherence peaks at $\omega = -(f + \omega_S)$ are an indication of possible effects which remain. Analyses of shear obtained from current meters must therefore be done with some caution to avoid erroneous results due to these effects.

REFERENCES

- Amorocho, J. and J. J. DeVries, A new evaluation of the wind stress coefficient over water surfaces, Journal of Geophysical Research, 85, 433-422, 1980.
- Bell, T. H., Radiation damping of inertial oscillations in the upper ocean, Journal of Fluid Mechanics, 88 289-308, 1978.
- Bendat, J. S. and A. G. Piersol, Random Data: Analysis and Measurement Procedures, Wiley-Interscience, John Wiley and Sons, Inc., New York, 1971.
- Fofonoff, N. P. and Y. Ercan, Response characteristics of a Savonius rotor current meter, unpublished manuscript, Woods Hole Oceanographic Institution Ref. 67-33, 1967.
- Gargett, A. E., P. J. Hendricks, T. B. Sanford, T. R. Osborn, and A. J. Williams III, A Composite Spectrum of Vertical Shear in the Upper Ocean from the Profilers EMVP, SCIMP and CAMEL, Pacific Marine Science Report 80-11, Institute of Ocean Science, Sidney, B. C, 1980.
- Gonella, J., A rotary-component method for analysing meteorological and oceanographic vector time series, Deep-Sea Research, 19, 833-846, 1972.
- Grabowski, W. J., Modeling of internal-wave induced shear: progress report, OPD TN-80-201-01, Ocean Physics Division, Science Applications, Inc., McLean, Virginia, 30 pp., 1980.
- Grabowski, W., and F. C. Newman, Spectral Model Predictions of Mean-Square Distortion Rates, Ocean Physics Division, Science Applications, Inc., McLean, VA. Technical Report SAI-82-485-WA, 1981.
- Halpern, D., R. A. Weller, M. G. Briscoe, R. E. Davis, and J. R. McCullough, Intercomparison tests of moored current measurements in the upper ocean, Journal of Geophysical Research, 86, 419-428, 1981.
- Koopmans, L. H., The Spectral Analysis of Time Series, Academic Press, New York, 1974.
- Krauss, W., The erosion of a thermocline, Journal of Physical Oceanography, 11, 415-433, 1981.

References (continued)

- Munk, W.. Internal waves and small-scale processes. Chapter 9 in Evolution of Physical Oceanography, Eds. B. A. Warren and C. Wunsch, MIT Press, Cambridge, Mass., 1981.
- Patterson, S. L., F. C. Newman, D. M. Rubenstein, and R. B. Lambert, Jr., Spatial distribution of vertical shear, SAI-82-294-WA, Ocean Physics Division, Science Applications, Inc. McLean, Virginia, 137 pp., 1981.
- Pollard, R. T., Properties of near-surface inertial oscillations, Journal of Physical Oceanography, 10, 385-398, 1980.
- Pollard, R. T. and R. C. Millard, Comparison between observed and simulated wind-generated inertial oscillations, Deep Sea Research, 17, 813-821, 1970.
- Pollard, R. T., R. B. Rhines, and R. O. R. Y. Thompson, The deepening of the wind-mixed layer, Geophysical Fluid Dynamics, 3, 381-404, 1973.
- Pollard, R. T., and S. Tarbell, A compilation of moored current meter and wind observations, Volume VIII (1970 array experiment), unpublished manuscript, Woods Hole Oceanographic Institution Ref. 75-7, 1975.
- Regal, R. and C. Wunsch, M_2 tidal currents in the western North Atlantic, Deep Sea Research, 20, 493-502, 1973.
- Rubenstein, D. M., Models of near inertial vertical shear, Technical Report SAI-82-546-WA, Science Applications, Inc., Ocean Physics Division, McLean, VA.
- Rubenstein, D. M., A dynamical model of wind-induced near-inertial motions, SAI-82-598-WA, Ocean Physics Division, Science Applications, Inc., McLean, Virginia, 55 pp., 1981.
- Rubenstein, D. M., A model of vertical dispersion of inertial waves in the upper ocean, SAI-83-861-WA, Ocean Physics Division, Science Applications, Inc., McLean, Virginia, 81 pp., 1982.
- Thorpe, S. A., The excitation, dissipation, and interaction of internal waves in the deep ocean, Journal of Geophysical Research, 80, 328-337, 1975.

References (continued)

Weller, R. A., Observations of the velocity response to wind forcing in the upper ocean, Journal of Geophysical Research, 86, 1969-1977, 1981.